IEEE Access
Multidisciplinary ⋮ Rapid Review ⋮ Open Access Journal

Received 3 February 2023, accepted 17 March 2023, date of publication 20 March 2023, date of current version 24 March 2023.

Digital Object Identifier 10.1109/ACCESS.2023.3259725

RESEARCH ARTICLE

Evaluating RF Hardware Characteristics for Automotive JCRS Systems Based on PMCW-CDMA at 77 GHz

MAXIMILIAN LÜBKE, (Member, IEEE), YANPENG SU, (Member, IEEE), AND NORMAN FRANCHI, (Member, IEEE)

Chair of Electrical Smart City Systems, Friedrich-Alexander-Universität Erlangen-Nürnberg, 91058 Erlangen, Germany

Corresponding author: Maximilian Lübke (maximilian.luebke@fau.de)

The authors acknowledge the financial support by the Federal Ministry of Education and Research of Germany in the project "Open6GHub" (grant number: 16KISK005).

ABSTRACT Joint communications and radar sensing (JCRS) applications are currently being hailed as the innovation of the next generation of mobile communications. The combination of communications and sensor technology on one hardware platform offers various advantages, such as significant savings in space and costs. The two technologies are no longer being optimized and developed side by side, as has been the case in the past, but jointly. The physical channel is used by both simultaneously, including the transmitter and receiver structures, which must be optimized for the combined application. This inevitably leads to an influence on the performance of both systems. In this work, this influence is considered and analyzed with respect to the effects of the radio frequency components. For this purpose, our previously published code-division multiple access (CDMA)-based and vehicle-to-vehicle-focused model is extended to a JCRS model and evaluated according to the achieved bit error rate as well as the mean deviation of the detected distance and velocity in Simulink. The influence of the non-ideal hardware components (mixers, power amplifier, low noise amplifier, filter, antenna) and characteristics (S-parameters, non-linearity of the amplifiers and the noise) on the sensing and communications are analyzed and compared in this automotive context. The results reveal that the noise of the low noise amplifier at the receiver side has the most decisive influence. In contrast, the noise generated by the power amplifier at the transmitter has no effect due to the relatively high signal power. The non-linearity of amplifiers at the transmitter also significantly impacts the available sensing range by limiting and compressing signal power. Besides, the phase noise with a frequency offset higher than 10 MHz can increase the communications and sensing error rate. In contrast, the influence of S-parameters is negligible, as the performance of communications and sensing is almost unchanged with different S-parameters. In the future, the proposed single-target scene will be further extended to a multi-target one.

INDEX TERMS CDMA, connected vehicles, joint communications and radar sensing, RF hardware characteristics, modeling, physical layer, PMCW, 77 GHz.

I. INTRODUCTION

In the last decades, communications and sensor technology were developed and optimized side by side [1]. Short-range radars operate at the frequency band of 77-81 GHz, while the 76-77 GHz frequency band has been assigned for long-range radars [2]. With the development of communications to ever higher frequencies in order to use the wide bandwidth available there, the focus is on combining the two technologies. So-called Joint communications and radar sensing (JCRS) approaches attempt to create a combination of the two to take advantage of their convergence. In particular, this is discussed for JCRS, i.e. the merging of communications signal and radar sensing, as they are very similar in terms of

The associate editor coordinating the review of this manuscript and approving it for publication was Xujie Li.

the underlying physical effects and consequently, the applied architectures [3]. Therefore, the joint concept includes using the same waveform on the same hardware platform, which in turn leads to a significantly reduced space requirement as well as minor hardware costs. This makes the approach extremely attractive for automotive manufacturers. Besides, JCRS is receiving particularly high attention, as future communications systems are foreseen to establish sensing as a service [4], [5]. Cui et al. summarize the benefits of JCRS systems or more generally expressed as Integrated (radar) Sensing and Communications (ISAC) or Joint Communications and Sensing (JC&S) systems [6]: According to them, the advantages of efficiency, which in addition to improvements in spectral and hardware efficiency also includes an increase in energy efficiency, are a strong argument in favor of JCRS applications in today's sustainability. However, the optimal waveform and hardware platform for both technologies, which allow joint operation in the current radar frequency ranges at 77 GHz, are still under discussion in the current literature [7], [8], [9], [10], [11], [12], [13]. This discussion is taken up and addressed in this work. Finally, a phase-modulated continuous waveform (PMCW) – code-division multiple access (CDMA) based JCRS system design is chosen, especially due to the advantageous interference properties.

The focus of the present work is primarily on the hardware components and their corresponding impairments of a combined JCRS system architecture. The impact of the non-idealities on the performance of the communications in terms of achieved bit error rate as well as that on the performance of the sensor system in terms of the mean deviation of distance and velocity detection are investigated. This includes the impact of characteristic quantities of the transmitter and receiver RF components (mixers, amplifiers, filters, antennas) and evaluates the observations of Rappaport et al. [14], [15], who highlight the rapid degradation of key transceiver performance metrics (noise figure and linearity of the low-noise amplifier; peak output power and power-added efficiency of the power amplifier) and, at the same time, the increase in phase noise for increasing carrier frequencies, typical for millimeter wave (mmWave) systems.

The underlying communications model has already been presented by the authors for vehicle-to-vehicle (V2V) communications and discussed with respect to the individual components in [16] and in the recently published work [17]. In the former one, a basic V2V communications model was introduced and evaluated for various modulation schemes. Building up on this, the latter publication already contained the mapping of the entire physical channel, including the representation of the radio frequency (RF) hardware components, the realistic channel (obtained from deterministic channel simulations for typical traffic scenarios), an interleaved or parallel transmission strategy, as well a wide variety of signal processing steps at the receiver. Besides, in [18], the authors showed the first evaluations of the combined communications and sensing model, which is extended and combined in this work with the previous progress. The resulting freely available model[1] ([19]) is capable of an extended radar sensing model in addition to the communications model to obtain a complete, combined system architecture for future JCRS applications.

The importance of considering hardware limitations in the design of future mmWave communications systems is addressed in current publications [20], [21]. According to Yang et al. [20], those hardware constraints result, inter alia, from manufacturing errors and introduce different hardware imperfections including phase noise, power amplifier nonlinearities, in-phase - quadrature-phase imbalance, etc., especially in mmWave frequencies. Wu et al. [21] state that a thorough performance analysis taking into account the impact of hardware impairments is needed to verify whether it will be possible to guarantee future ultra-reliable low-latency communications. Besides, Bartoletti et al. [22] predict in their outlook that hardware impairments start to dominate positioning and sensing performance, which, in the inclusion of the above, again emphasizes the relevance of those for future JCRS systems. A similar statement is made by Wymeersch et al. [23], who also assign a high value to the question of understanding how hardware errors affect localization and detection accuracy and how signals should be designed to make estimation robust to hardware errors. Accordingly, there is great interest in investigating these hardware impairments, as highlighted, for example, in the European 6G flagship project Hexa-X [24].

Those hardware challenges, also addressed by Bozorgi et al. [25] and Oliveira et al. [3] for both radar- and communication-centric JCRS systems working in the 77 GHz range, such as linearity and efficiency of power amplifiers (PAs) and low noise figure, high gain, and compression point in low noise amplifiers (LNAs) are taken up and extended by further hardware impairments such as non-ideal S-parameters in the proposed work. Our contributions can be summarized as follows:

- Discussing potential JCRS waveforms and then selecting a PMCW-CDMA-based system design due to its benefits compared to frequency-modulated continuous waveform (FMCW) or orthogonal frequency division multiplexing (OFDM) based ones;
- Extending the previously published V2V communications model to a JCRS one, containing the whole physical layer (including the RF hardware representations, the channel and the digital signal processing blocks for the sensing as well as the communications part;
- Evaluating the impact of the RF hardware non-idealities, concerning S-parameters, (phase) noise, and non-linearity of the amplifiers on simultaneously the communications (bit error rate) and sensing performance (average distance and velocity error, respectively);

[1] https://doi.org/10.5281/zenodo.7352183

- Discussing the design recommendations and criteria for future JCRS systems based on the former metrics;
- Providing the models freely to the public so everyone can participate.

The publication is structured as indicated hereafter: In chapter II, potential JCRS waveforms are presented and discussed in terms of their suitability for automotive applications. In addition, the state-of-the-art JCRS modeling, mainly taking hardware impairments into account, is reviewed, and the contribution of the proposed publication is highlighted. Subsequently, the description of the developed JCRS system model follows in chapter III. On the one hand, a summary of the extension of the communications model (published in [17]) is given; on the other hand, the radar sensing part is introduced. However, this work focuses on the hardware components and their corresponding non-idealities. The metrics to compare their effects on the communications and sensing performance are provided in chapter IV. The hardware impairments themselves are described in chapter V and analyzed with regard to their influence on communications and radar performance. This evaluation takes place in chapter VI, while the discussion of the results follows in chapter VII. In the last chapter, the work is summarized, classified in the state-of-the-art and finally, an outlook is provided.

II. STATE-OF-THE-ART OVERVIEW

In this study, JCRS systems are investigated with particular emphasis on radar-based communications. Radar is a well-known technology in the automotive sector and is now built as standard in vehicles for applications such as adaptive cruise control or advanced driving assistant [2]. In contrast to camera systems, radar offers the great advantage that the sensing capabilities are not affected by sunlight or adverse weather conditions. Besides presence detection, radar can also measure distance, speed and, in the case of multi-antenna systems, the separation of objects in space.

Current systems are mostly based on a waveform called FMCW. However, this waveform is under considerable discussion, especially due to the high interference to be expected, justified by the ever-increasing number of vehicles equipped with radar sensors with a simultaneous increase in the number of radar sensors in a single vehicle [26], [27]. Consequently, and especially in the context of future JCRS systems, various waveforms are under consideration, which in turn are well known from communications, such as OFDM or CDMA-based systems. A comparison of different waveforms is accordingly addressed in the following.

In addition to the choice of the underlying waveform, developing future JCRS systems is a generally complex and costly process. Known for example from the antenna design, the vehicle manufacturers and the suppliers of the sensors/antenna systems must be in close contact with each other. Therefore, in order to replace the laborious trial-and-error approaches, simulation-based analysis is preferred [28]. An overview of current modeling approaches is provided, especially with regard to hardware impairments and their impact on the overall system performance.

A. DISCUSSION OF JCRS WAVEFORM

FMCW is the state-of-the-art waveform used in the current automotive radar sensors and impresses with its underlying signal processing. The desired target parameters (velocity, range, spatial orientation) can thus be determined easily and cost-effectively by means of the fast Fourier transform (FFT). At the same time, FMCW radars are usually operated without a focus on multiple access techniques. Accordingly, Waldschmidt et al. [2] state that interference especially becomes problematic for FMCW systems with the increased number of sensors since no rules for coexistence are available at 76 – 77 GHz or 77 – 81 GHz. This in turn results in the susceptibility of FMCW systems to interference when the interference falls within the receiver's passband. This case is more likely to occur in dense traffic scenarios, where with the increasing number of vehicles and the increasing number of sensors on a single vehicle, the interference problem is further amplified [26], [27]. However, the interference needs to be minimized as it can end up in critical traffic scenarios due to the failed communication of safety-related information and can lead to reduced measurement accuracy, detection of ghost targets, or even complete failure of the sensor system [2]. Furthermore, it has been shown that by means of spoofing attacks, FMCW radar systems are prone to be disrupted in such a way that even critical accidents can be induced by affecting the vehicles' sensors [29], [30]. Consequently, as FMCW is used in radar sensor technology today (non-standardized, noisy, and susceptible to interference), it is considered critical or even unsuitable for communications purposes, since a distortion-free signal is required for the communications of safety-relevant information.

PMCW is considered a promising alternative continuous waveform, which utilizes a direct sequence code division multiple access (DS-CDMA) code division multiplexing and thus does not use a linear frequency ramp, unlike FMCW approaches. Instead, the processing is performed using correlation receivers, which allows for a simple, energy-efficient, and robust implementation that in turn avoids fast frequency synchronization and the generation of highly linear edges [31], [32]. Additionally, PMCW-based systems are less susceptible to carrier frequency deviations than OFDM-based multi-carrier systems. High-frequency deviations arise in OFDM due to the need for multiple local oscillators and leakage effects of the discrete Fourier transform, which in turn requires the implementation of correction algorithms. Besides, OFDM-based systems have the disadvantage of high dynamic range in the transmitted envelope power. Consequently, a poor peak-to-average power ratio (PAPR) is exhibited [33], [34]. The demands on the amplifiers are correspondingly high since a high dynamic range must be linearly amplified to avoid nonlinear distortion. At the same time, the quantization stages of the

digital/analog (D/A) converters or analog/digital (A/D) converters are not optimally utilized, since a large part of the resolution of the converters is reserved for the rare peak values. Moreover, the autocorrelation property of OFDM signals cannot be guaranteed for quadrature amplitude modulation (QAM) constellations, resulting in sidelobes that degrade the detection performance [35], [36], [37]. In contrast, the PMCW-based single carrier approach used here is able to maintain low PAPR values, which is essential for mmWave systems equipped with imperfect nonlinear devices.

B. MODELING

Simulation models are partially available in the literature for vehicular communications [38], [39], [40], [41], [42], [43], but most of them refer to the sub-6.GHz V2V: Reichardt et al. [38] designed a system at 5.9 GHz and investigated, inter alia, the bit error rate (BER) and the packet error rate (PER) for V2V communications in different traffic scenarios. Shirude et al. [39] evaluated a transmitter and receiver design using MATLAB/Simulink, Wang et al. [40] published a simulation environment for ad hoc networks (VANET) reconstructing inter-vehicle communications for different scenarios using MATLAB. Dakić et al. [41] presented a validated real-time modeling of a vehicular communications scenario at 5.9 GHz using a hardware-in-the-loop simulation platform and a geometry-based stochastic channel model. Saponara and Gagliardi [42] proposed a physical layer model for communications based on IEEE 802.11p using Matlab/Simulink simulations to analyze the baseband processing, the physical channel for different scenarios (urban, suburban, highway) and the RF hardware. In the same vein, the work carried out by Cabezas et al. [43] presented a simulation model of the physical layer for IEEE 802.11p. This allowed the authors to evaluate the PER. Alternative standards to the 802.11p standard are discussed by Triwinarko et al. in their developed models [44]. As a result, Triwinarko et al. observed improvements in the physical layer (in terms of improved PER and partially higher throughput) in other 802.11 standards.

In the publications [38], [40], [41], [43], [44] mentioned above, the physical layer is examined on the bit level, as for example in [41] by a hardware-in-the-loop setup, however, the hardware influences remain without consideration. Shirude et al. [39] used RF blocks similar to the proposed work, but did not specify what settings they made, so ideal conditions are assumed for the hardware blocks. Furthermore, Saponara and Gagliardi [42] built an analog transmitter and receiver in Simulink and considered the hardware impairments: receiver noise figure, receiver sensitivity, transmitter and receiver oscillator phase noise and the implementation loss factors of the digital base-band. However, they used specific configurations for their included hardware impairments and thus, did not vary them, as is the case in the present work, which aims to study their effects in detail. In summary, most of the above systems did not consider, or only partially considered, hardware impairments of the communications or JCRS systems and their potential performance degrading effects [42].

This in turn must be seen critically, as the hardware effects have a significant impact on the performance of the communications and sensor technology and therefore cannot be ignored. Oliveira et al. [3] address these hardware challenges, listing the following four aspects: First, the linearity and efficiency of the PAs; second, the in-band full-duplex operation (IBFD) of the transmit and receive channels with sufficient isolation; third, the low noise figure, the high gain, and the compression point in the LNAs; and fourth, the high-resolution D/A converters and high-resolution A/D converters in all-digital JCRS systems. Some effects, such as clock synchronization, are not problematic for communications, but lead to considerable errors on the part of the sensor system. Asynchronous transceivers and their negative effect on radar performance were addressed, for example, by Zhang et al. [45]. Bozorgi et al. [25] analyzed transceiver block requirements, in terms of amplifiers (PA, LNA) and voltage-controlled oscillators (VCO) or phased-locked loops (PLL) for a modulated FMCW waveform for future JCRS systems at frequencies of 70 – 83 GHz. The theoretical analyses of the RF front-end challenges and possible ways to converge the requirements in a single transceiver presented by Bozorgi et al. are explored in detail in the present work.

Barreto et al. [46] investigated the effects of hardware imperfections for an underlying FMCW waveform at 61 GHz, while focusing on the impact of non-linearities of the LNA and PA on the communications performance, considering perfect synchronization and a single-path channel without fading. Likewise, for FMCW-based system architecture, Dudek et al. [47] investigated the effects of realistic nonlinear hardware components on the down-converted baseband signal for a long-range radar at 77 GHz. Dudek et al. concluded that the need for implementing accurate nonlinear component models is imperative as in their evaluated scenarios the receiver magnitude is limited to about 2 dBm and the noise floor is about 20 dB higher for close targets, which gets especially critical in a blocking scenario where a smaller target cannot be detected anymore due to the supersaturated receiver circuit.

Chen et al. [48] considered an OFDM-based localization system at 140 GHz, taking hardware impairments into account and investigating the contribution of each individual impairment. They focused on residual phase noise (PN) and residual carrier frequency offset (CFO), residual mutual coupling (MC) and power amplifier nonlinearity (PAN). In their conclusion, PN and PAN affect both angle and delay estimation, whereas CFO and MC have a more significant effect on angle estimation. Hence, they advised special pilot signal design, hardware degradation estimation, and mitigation algorithms for accurate localization in 6G systems.

However, to the best of the authors' knowledge, there are hardly any observations for the impact of hardware impairments for a direct-sequence spreading

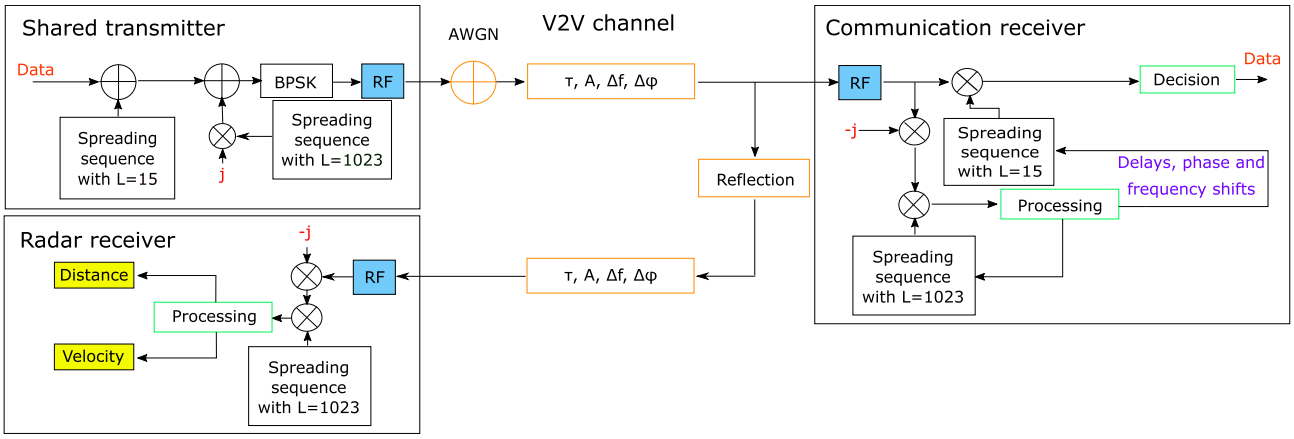

FIGURE 1. Proposed JCRS system architecture based on PMCW-CDMA at 77 GHz. As an extension to our previously published contribution [17], which focused specifically on V2V communications, the radar part has now been included and the performance of both was evaluated with respect to RF impairments.

spectrum (DSSS)-based PMCW waveform, including non-perfect synchronization. This is also the conclusion reached by Adler et al. [49] in their analysis of the current modeling tools. They introduced their developed, so-called HermesPy, open-source link level evaluator, which is capable of modeling the communications as well as radar for various waveforms, including also single carrier ones. Our work extends this detailed modeling by focusing even more on the effects of hardware impairments such as S-parameters, phase noise, amplifier non-linearities, and noise in general on communications and sensing performance at frequencies in the 77 GHz range.

Remark 1: The layers above the physical layer (according to the Open Systems Interconnection model) are not the focus of this work, but are no less important for the realistic modeling of communications or JCRS systems. That is why a brief outline of current developments is given below. There are various network simulators such as OMNET++, ns-3, OPNET, JiST/SWANS and GloMoSim. Veins, based on OMNET++ and the traffic simulator SUMO [50], or Artery, a modular V2X framework based on ETSI ITS-G5 protocols [51], are well-known examples of simulation software that provide the link between physical and network layers. To give two examples that meet the requirements of mmWave-based vehicle communications for 5G networks: In [52], MilliCar (an ns-3 module based on the latest NR V2X specifications [53]) was used to evaluate the performance of V2V networks. MilliCar contains the implementation of the 3GPP channel model for V2V communications, while aligning the physical layer with the medium access control (MAC) layer within the 3GPP NR V2X framework. Besides, the simulation of vehicular networks can also be implemented in Matlab/Simulink, as shown in [54]. Here, Storck and Duarte-Figueiredo presented a study on 5G VANETs comparing the results (transmission rate and transmission delay) of ns-3 and Matlab simulations. In the future, we also plan to integrate the proposed model into the Veins network simulator to gain insight into the higher layers and their impact on JCRS performance.

III. JCRS MODEL

Based on [17], where the authors presented and tested a mmWave simulation system for vehicular communications at 77 GHz, this model is extended to include the radar detection function. The obtained JCRS system is radar-based since the waveform is PMCW, and automotive radar systems occupy an operation frequency of 77 GHz. The radar system shares the same hardware, spectrum, waveform, and signal with the communications part.

A typical V2V scenario containing two cars is examined in the following. One car acts as a transmitter of the evaluated JCRS signal, which is later used for communications with the (other) receiving car and monostatic sensing by the transmitting car itself. On the one hand, the communications receiver vehicle is capable to estimate the channel state information and extract the communicated data afterward. On the other hand, the signal is reflected by the communications receiver vehicle and then received by the transmitting vehicle again. At the transmitter, the reflected signal is used to estimate the relative direction, distance and velocity of the environment (in our case the communication partner vehicle). Consequently, one signal sequence can competent both communications and sensing functions and benefit from the saved spectrum and energy. In Fig. 1, the proposed system structure is depicted, which will be reviewed regarding the communications system, the channel model as well as the newly introduced modeling of the radar sensing part with its underlying signal processing steps.

A. COMMUNICATIONS

1) ARCHITECTURE

The shared transmitter is capable of implementing communications and sensing functions simultaneously. The JCRS system uses a single carrier waveform with direct-sequence spreading spectrum (DSSS): the data sequence, generated by a randomly but equally distributed Bernoulli Binary generator, is spread using a short spreading sequence with a length

of $L = 15$. In addition, a long spreading sequence with a length of $L = 1023$ is chosen as the pilot signal to achieve a more precise channel estimation and extend the maximum unambiguous range. Hereby, the spreading sequences are known as pseudo-random noise (PRN) sequences due to their random-like nature. There are different types of PRN sequences, like maximum length sequences (m-sequences), Gold sequences [55], Walsh-Hadamard codes [56] and Barker codes [57]. In this work, m-sequences generated by linear feedback shift registers (LFSR) are chosen as the spreading sequences because of their simple generation process and good auto-correlation function (ACF) and cross-correlation function (CCF) performance, which helps to reduce the distortion and interference from other transmitters [58].

Moreover, the transmitter uses a parallel approach: the data sequence is directly transmitted on the in-phase (I) component, while the pilot is transmitted over the quadrature (Q) component by a 90° phase shift. At the receiver, both components are separated by the despreading process. The advantage of this parallel approach is that both the communications and radar receivers can keep track of the channel, especially for the radar function, which is expected to react immediately to the change of channel conditions.

The spread signal is modulated by a binary phase shift keying (BPSK), in order to avoid interference between the I and Q components. Afterward, the modulated signal is processed in the RF blocks: Mixed to 77 GHz, filtered, amplified and transmitted with the antenna. At the receiver, the signal is collected by the antenna and then amplified, filtered and mixed down. In the baseband, the pilot and data sequences are processed separately. The channel information like delay, phase and frequency shifts are extracted from the pilot and used to compensate for the channel to get reliable data demodulation and detection.

2) EXTENSION OF [17]

The basic architecture of the communications was taken from the authors' previous publication [17], but the parameters were further adapted to match future JCRS applications. Tab. 1 lists the old configurations as well as the ones used in this work. Considering the large available bandwidth for mmWave, the bandwidth is set to $B = 4\,\text{GHz}$, whereas the corresponding chip rate is $R_\text{c} = 2\,\text{Gbit/s}$. The spreading gain G stays at 40. Thus the data rate is $R_\text{T} = 50\,\text{Mbit/s}$.

In addition, the architecture was adapted to the single-input single-output (SISO) antenna arrangement and the simplified 1-path channel model, which is described in more detail in the next subsection. Thus, the maximum-ratio combing and the Rake-receiver structure were not considered and were reduced to one single finger in this work.

As for the channel estimation part, the function of the synchronization block and the despreading part are overlapped, since both contribute delay compensation. Moreover, as the synchronization changes the time shift of the locally generated PRN sequence, it also influences the estimated delay in despreading. To this end, the synchronization part is removed.

TABLE 1. Overview of the system parameters.

Parameter	Old [17]	New
Carrier frequency f_c	77 GHz	
Data rate R_T	5 Mbit/s	50 Mbit/s
Chip rate R_c	200 Mbit/s	2 Gbit/s
Code length L	1023	
Spreading gain G	40	
Bandwidth B	400 MHz	4 GHz
Modulation	BPSK	
Multiplexing	DSSS	
Spreading sequence	m-sequence	
Maximum unambiguous range	767.25 m	76.725 m
Range resolution	0.75 m	0.075 m
Maximum unambiguous velocity	–	171.38 km/h
Velocity resolution	–	0.186 m/s

Moreover, the radar receiver and the corresponding reflection path are included in the system. The echo experiences the same delay, attenuation and frequency shift as the forward signal. The radar receiver extracts channel information from the echo signal. With the increased chip rate and the fixed sequence length, the maximum unambiguous range is reduced while the range resolution is improved. Additionally, the Doppler shift is estimated using FFT instead of the phase derivative proposed in [17]. Therefore, the maximum unambiguous velocity and velocity resolution are defined.

B. CHANNEL

The channel characteristics are extracted from WinProp, a 3D-Ray-Tracing software solution provided by Altair, and have already been integrated for a typical traffic scenario in [17]. It should be noted that WinProp was validated for use in the 77 GHz frequency range by the authors in [59]. In this work, an line-of-sight (LOS) scenario is considered, in which two vehicles communicate with each other while using the reflection on the communication partner for radar sensing. Thus, the radar performance of detecting a single object is investigated, and for simplification, only the direct path is included. Multipaths or a non-Line-of-Sight (NLOS) scenario are left for future research. Besides, the channel characteristics, like delay, attenuation, additive white Gaussian noise (AWGN), and Doppler frequency shifts (f_D), are included. The channel parameters are summarized in Tab. 2.

Since the communications and the sensing share the same signal waveform, the signal arrives at the receiver of the communication partner vehicle and is simultaneously reflected to the original transmitter car. The wave travels through the same channel back again and is finally received by the transceiver. As a result, the delay and the Doppler shift are doubled, and the path loss is also increased. Moreover, the reflection also leads to a reflection gain and a phase shift $\Delta\phi$. The reflection gain is usually specified as radar cross section (RCS) σ with the unit area (m^2) or decibels with

TABLE 2. Communication channel parameters of the LOS path.

Parameter	Delay τ	Attenuat. A_c	f_D	σ	$\Delta\phi$
Value	67.6 ns	96.31 dB	5.1 kHz	15 dBsm	90°

respect to 1 square meter (dBsm). It is mainly determined by the object's size, shape and material, as well as the signal frequency, polarization and incidence angle. For cars, the RCS is typically 10 to 20 dBsm [60], whereas in this work, σ is chosen to be 15 dBsm.

Remark 2: The communication attenuation of the LOS path can be back-calculated by

$$A_c = \frac{G_t G_r \lambda^2}{(4\pi)^2 R^2}, \tag{1}$$

where G_t and G_r are the transmitter and receiver antenna gains, respectively, $\lambda = \frac{c}{f_c}$ corresponds to the signal wave length and R is the propagation distance. In this scenario, the distance between the transmitter and the receiver is $R = 20.28$ m, resulting in a corresponding path loss of 96.31 dB (without considering the antenna gains). However, for the radar signal path loss, according to the radar equation

$$A_r = \frac{G_t G_r \lambda^2 \sigma}{(4\pi)^3 R^4}, \tag{2}$$

the radar signal attenuation A_r is 118.44 dB (again without taking the antenna gains into account).

C. RADAR

1) ARCHITECTURE

At the radar transceiver, the sensing information (like distance and relative velocity and, in multi-antenna systems angle of arrival (AoA)) is extracted from the reflected signal. Generally, only the pilot signals are used for this purpose, with processing similar to the channel estimation in the communications receiver: After despreading the pilot, the delay and the Doppler frequency shift are extracted, depicted in Fig. 1. A correlation bank is implemented to estimate the delay and frequency offset: after correlation, the highest peak in the correlation bank is interpreted as the searched despread pilot, whose index indicates the propagation delay and its phase carries the information about the phase and frequency shifts. In this work, the Doppler frequency shift is calculated by the FFT. At last, the distance and the relative velocity are estimated according to

$$d = \frac{c \cdot \tau}{2}, \tag{3}$$

$$v = \frac{c \cdot f_D}{2 f_c}, \tag{4}$$

where $c = 3 \times 10^8$ m/s corresponds to the speed of light in vacuum, τ to the propagation delay, and $f_c = 77$ GHz to the carrier frequency.

The estimation methods of AoA are usually based on multiple-input multiple-output (MIMO) radar designs and have been proposed in other reports like [61] and [62]. In this work, a SISO system architecture is chosen to focus on the evaluations of the impact of hardware impairments on the range and velocity estimations. The consideration of AoA is left for future studies.

In the proposed JCRS system, communication is based on the radar sensing signal, which helps to improve the spectrum efficiency, reduce the hardware size and save energy. The pseudo-random-like nature of the PMCW signals does make it harder to be detected by other devices and in consequence, more challenging to be actively jammed. Overall, the PMCW signal can efficiently reduce inter-user and inter-channel interference, improving the communications' safety and sensing reliability.

2) SIGNAL PROCESSING

The basic signal processing steps are already included in the previous work [17] in the context of estimating the channel state information for the V2V communications system. However, those concepts can be reused for radar sensing, where a correlator bank despreads the pilot and extracts the delay and phase offset of the received signal. The frequency shift is then estimated by deriving the phase. This frequency shift estimation strategy is advantageous due to its fast response time, which can prevent data loss at the beginning of communications. However, it is fragile and unstable to noise. Moreover, if two objects have the same distance (i.e., same delay) to the transceiver, the frequency estimator cannot distinguish their respective Doppler frequencies: the frequency estimator only gets one result, which is the superposition of those two frequencies. Hence, the most common frequency/relative velocity estimation scheme is based on the FFT, as it can extract all frequency offsets from the spectrum. That is why it is preferred in radar sensing.

Fig. 2 shows the applied radar signal processing scheme, which is well-known in the state-of-the-art literature [63], [64]. The decorrelator extracts the delay and despreads the pilot to calculate the distance and relative velocity, respectively. The accumulator accumulates M correlation results to increase the signal-to-noise ratio (SNR). Afterward, the N-FFT takes N samples to estimate the frequency offset. The total dwell time T_d is calculated by

$$T_d = L \cdot T_c \cdot M \cdot N, \tag{5}$$

where $L = 1023$ is the length of the pilot sequence, T_c is the chip period with $T_c = \frac{1}{R_c} = 0.5$ ns. Note that the dwell time is the theoretical latency of the frequency estimation, while the frequency resolution Δf is inversely proportional to the dwell time:

$$\Delta f = \frac{1}{T_d}. \tag{6}$$

An enhanced velocity resolution leads to a higher latency and vice versa, which is why a suitable trade-off has to be identified.

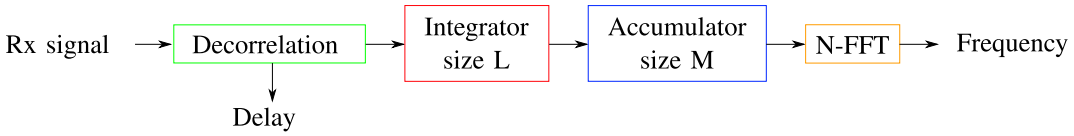

FIGURE 2. Signal processing chain of the PMCW-based radar: The delay is calculated after decorrelation, while the Doppler shift is estimated by an FFT.

3) UNAMBIGUOUS RANGE AND RANGE RESOLUTION

The maximum unambiguous range defines the theoretical maximum distance that the sensor can detect. The unambiguous range is determined by the period of the pilot since if the reflected pilot of the previous period is detected after the start of the next period, the detected time delay is $L \cdot T_c$ less than the correct value [65]. Thus, the maximum unambiguous range r_u is defined as

$$r_u = \frac{c \cdot L \cdot T_c}{2}. \tag{7}$$

In this work, r_u equals 76.725 m, meaning that the radar is specified as a short-range radar. However, it is possible to extend the unambiguous range by increasing the pilot PRN sequence length L.

The range resolution Δr denotes the minimum distance between objects that the radar can still distinguish [66]. The sensing resolution determines the sensitivity and the achievable sensing accuracy. The range resolution is related to the chip rate,

$$\Delta r = \frac{c \cdot T_c}{2}. \tag{8}$$

According to Eq. 8, the range resolution can be improved by employing a large bandwidth, which is naturally available at mmWaves frequencies. For the chosen bandwidth of 4 GHz, this results in a range resolution of 0.075 m in the proposed system.

Remark 3: The maximum unambiguous range denotes a theoretical maximum available sensing range. However, other factors like channel attenuation and noise power also affect the maximum sensing range.

4) UNAMBIGUOUS VELOCITY AND VELOCITY RESOLUTION

The maximum unambiguous velocity defines the theoretical highest speed that the sensor can detect without ambiguity. The decision of maximum unambiguous velocity should refer to the radar application field and the corresponding requirements. As a short-range radar is considered, which is usually employed on urban roads, where the speed is limited to 50 km/h (13.9 m/s) in Germany and most countries, the maximum relative speed of two vehicles is 100 km/h (27.78 m/s). Thus, the unambiguous velocity v_u has to be higher than this value. It is given by

$$v_u = \frac{c}{4 \cdot f_c \cdot M \cdot L \cdot T_c}. \tag{9}$$

In this work, v_u equals 47.61 m/s (171.38 km/h), which is well over twice the maximum speed allowed on urban roads.

The velocity resolution Δv implies the minimum change in velocity that can be detected. Δv is proportional to the frequency resolution and, thus, inversely proportional to the dwell time T_d, i.e.,

$$\Delta v = \frac{c \cdot \Delta f}{2 f_c} = \frac{c}{2 \cdot f_c \cdot T_d}. \tag{10}$$

In [63], their PMCW system has a velocity resolution of 0.5 m/s, while in [65], the velocity resolution is $\Delta v = 0.25$ m/s. Moreover, in [32], their PMCW radar has a velocity resolution of 0.2 m/s. Due to the trade-off between accuracy and latency, $\Delta v = 0.2$ m/s is seen to be required in this work, resulting in a corresponding dwell time of $T_d = 10$ ms.

The FFT size N is given by

$$N = 2^{\lceil \log_2 \frac{2 v_u}{\Delta v} \rceil} = 512. \tag{11}$$

Since $N = 512$, $T_d = 10$ ms, $L = 1023$, $T_c = 0.5$ ns, according to Eq. 5, $M \geq 39$ is desired. In this work, M is set to 40. Thus, the dwell time T_d, also called latency, is recalculated to 0.0105 s. According to Eq. 10, the velocity resolution is recalculated to $\Delta v = 0.186$ m/s.

Remark 4: The sensing resolution denotes a theoretical minimum achievable sensing error. However, other factors, like environment and hardware quality, also influence the sensing error. Considering the sensing error may exceed the resolution due to these factors, other metrics to measure the sensing accuracy are required.

Remark 5: Tab. 1 lists the discussed system parameters. The transmission with DSSS benefits from suppressed interference and distortion. The large occupied frequency bandwidth allows a high data rate and range resolution. It is possible to increase the data rate by decreasing the spreading gain. However, this will degrade communications security. The maximum unambiguous range is proportional to the pilot sequence length. This range is in tens of meters in this work, allowing short-range sensing. Of course, it is possible to increase the pilot length by adding registers in the LFSR.

IV. METRICS

Since the impact of non-ideal hardware should be investigated, both communications and radar functionalities require metrics to evaluate their performance, especially the error rate. For communications, this includes an evaluation of the bit error rate (BER), while for the radar function, in order to measure the estimation performance, the mean absolute error (MAE) is utilized. In the following, these metrics are explained in more detail.

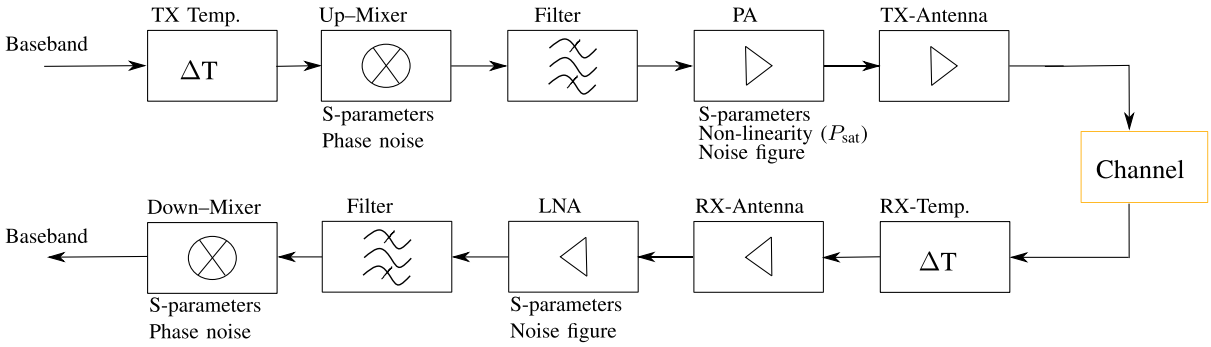

FIGURE 3. Applied RF signal processing chain with the varied parameters given below the corresponding hardware blocks.

A. COMMUNICATION–BER

The BER over the SNR is an important metric for measuring communications performance. In [17], the BER under different configurations has been investigated. Generally, the BER-SNR curve is a water-fall curve: the BER decreases with increased SNR. However, the impact of the non-ideal hardware components on communication performance is to be investigated in this work. Consequently, the BER is tested for different hardware parameters (like S-parameters, noise figure, etc.), instead of the BER-SNR curve.

B. SENSING–MEAN ABSOLUTE ERROR

Next to the resolution, other factors affect the sensing accuracy, like the attenuation and the noise level. As the MAE directly measures the accuracy of the sensing, it is chosen as the main performance metric for the radar system performance. Here, the range-MAE (R-MAE) r_{M} and velocity-MAE (V-MAE) v_{M} are defined by

$$r_{\mathrm{M}} = \mathrm{avg}|r_{\mathrm{d}} - r|, \tag{12}$$
$$v_{\mathrm{M}} = \mathrm{avg}|v_{\mathrm{d}} - v|, \tag{13}$$

where r_{d} and v_{d} correspond to the detected range and velocity, respectively. The actual range and velocity are indicated by r and v.

Similar to the BER, the MAEs also change with varying channel and hardware conditions. Longer distances, higher noise power or worse hardware quality lead to larger MAEs. Thus, the MAEs are considered suitable metrics to measure the impact of hardware effects on radar functionality. Summarized, in this work, the performance of communications is measured by the BER and the radar sensing accuracy is represented by the R-MAE and V-MAE.

V. ANALYSIS OF THE HARDWARE EFFECTS

The following RF components are integrated into the JCRS system under consideration: mixer, filter, amplifier and antennas, whose characteristic impairments will now be investigated in more detail. Their realistic parameters are integrated and can be varied according to the demands. The RF system design is depicted in Fig. 3, where the upper components denote the RF transmitter block, while the lower components represent the RF receiver block. The parameters (S-parameters, NF, PN, non-linearity parameters) whose impact on system performance is to be investigated are indicated below the corresponding RF components. These non-idealities were determined in [17] and were selected from the state-of-the-art literature for realistic 77 GHz RF devices [47], [67], [68], [69]. The operating temperature of both the transmitter and the receiver is fixed to 300 K. At the transmitter, the up-mixer converts the baseband signal to the RF carrier frequency of 77 GHz. Afterward, the signal is filtered by a bandpass LC-filter with a 3 dB bandwidth of 4 GHz centered at 77 GHz, whose characteristic is shown in Fig. 4 and the corresponding quality factor is given by $f_{\mathrm{c}}/B = 19.25$. The filtered signal is then amplified by a PA operating at 77 GHz with 26.4 dB gain and an output saturation power P_{sat} of 15.82 dBm. Additionally, an antenna block is included after the PA to model the antenna mismatch, whereas its parameters are chosen from [70]. The corresponding antenna gain is 16.56 dB. The antenna is installed at both the transmitter and receiver sides. The corresponding total antenna gain is 33.12 dBi.

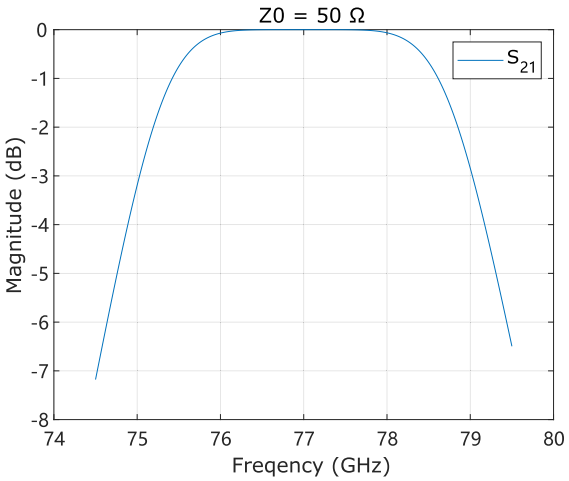

FIGURE 4. Characteristic of the applied bandpass filter with the center frequency of 77 GHz and 3 dB-passband of 4 GHz.

At the RF receiver, after being received by the antenna, the signal is processed by an LNA with a 10 dB gain, having

TABLE 3. RF parameters. The experiment comprises four parts: (1) The performance comparison between the ideal ($s_{11} = s_{22} = 0$) and non-ideal (listed in this table) S-parameters. (2) The test of the non-linear property of PA. (3) The investigation of PN of up- and down-mixers. (4) The separate implementation of noise figure (NF) of PA and LNA.

	s_{11}	s_{21}	s_{22}	IIP3	OP1dB	Noise
Up/Down-mixer [67]	-11.4 dB	2.1 dB	-16.1 dB	-1 dBm	-8.9 dBm	PN at [0.01,0.1,1,10] MHz: [-30,-58,-87,-115] dBc/Hz
PA [68]	-15 dB	26.4 dB	-3.9 dB	-13.9 dBm	11.5 dBm	NF: 10 dB
LNA [47], [69]	-25 dB	10 dB	-20 dB	2.2 dBm	1.6 dBm	NF: 5 dB

an NF of 5 dB. In the next step, the signal is filtered by a bandpass filter with configurations the same as the one on the transmitter side. At last, the signal is converted back to the baseband by the down-mixer.

The parameters of the RF components are listed in Tab. 3, where the S-parameters, the linearity like the third order intercept point (IP3) (here: input IP3 (IIP3)) and the 1 dB-compression point (P1dB) (here: output P1dB (OP1dB)), and the noise (phase noise of mixers and noise figure of PA and LNA) are included. In the experiment, their impact on the JCRS system is investigated, regarding the BER and the MAEs, as mentioned in the previous section. In this work, first, the effect of the S-parameters of individual components is investigated. Then the test of the phase noise of the mixers is implemented. Afterward, the non-linearity of the PA is chosen to analyze the influence of the non-linear properties. At last, the noise figures at the transmitter and receiver sides are handled separately. Besides, the co-effect of the PA's non-linearity, the noise generated at the receiver and their influence on the sensing range are described in detail.

A. S-PARAMETERS

The S-parameters represent the linear characteristics of the RF devices. For a two-port device, the S-matrix is a four-element matrix:

$$S = \begin{pmatrix} s_{11} & s_{12} \\ s_{21} & s_{22} \end{pmatrix}, \tag{14}$$

which describes the forward gain, reflection and isolation properties as follows:

- s_{11}: input port reflection
- s_{12}: reverse gain
- s_{21}: forward gain
- s_{22}: output port reflection

The reverse gain s_{12} is ignored due to its negligible values.

The S-parameters' operation frequency is 77 GHz in this publication. The S-parameters influence the communications and sensing results since the reflection parameters s_{11} and s_{22} bring the input and output return loss, leading to power reduction, whereas the reverse gain s_{12} corresponds to the feedback from the output to the input port and influences its stability and the forward gain s_{21}. Ideally, when $s_{11} = s_{12} = s_{22} = 0$, there is no wave reflection, and the reverse isolation is perfect. Consequently, the S-parameters have no bad influence on the system performance. However, realistic RF components have non-zero reflection parameters and their reverse isolation is not ideal. The BER and MAEs with ideal and non-ideal (realistic) S-parameters are compared in the experiment. Their difference indicates the influence of the S-parameters. Other RF parameters are idealized during the test to remove their influence.

The experiment for S-parameters is conducted for two SNRs, which are considered the upper and lower SNR limit for this system design since they can represent the system in good and bad environments. The SNR is calculated at the output of the RF down-converter and before the A/D-converter, where all of the analog noise is included. Since the channel characteristics are fixed, the SNR only changes with varying noise power at the receiver side.

According to

$$P_\mathrm{r} = \frac{P_\mathrm{t} G_\mathrm{t} G_\mathrm{r} \lambda^2 \sigma}{(4\pi)^3 R^4}, \tag{15}$$

where P_t denotes the signal power at the transmitter side and P_r the signal power at the receiver side. A maximum received signal power of $P_\mathrm{r} = -69.5$ dBm is achieved in the case of $P_\mathrm{t} = P_\mathrm{sat}$. As for the noise power, only the thermal noise and the noise generated by the RF receiver are considered. The noise power generated at the transmitter side can be ignored due to the high propagation loss. According to the world meteorological organization (WMO) report, the observed lowest and highest temperatures on the earth are -89.2°C and 56.7°C, respectively. Their corresponding thermal noise power is -79.93 dBm and -77.4 dBm for the applied bandwidth of 4 GHz. At the receiver, according to the Friis formula for noise factors [71]

$$F_\mathrm{total} = F_\mathrm{LNA} + \frac{F_\text{down-mixer} - 1}{G_\mathrm{LNA}}, \tag{16}$$

the total noise figure is mainly determined by the first RF block (the LNA), since $G_\mathrm{LNA} = 10$ dB is very high. The LNA's NF is set to 5 dB in this system, while the general LNAs have NF lower than 10 dB [47], [69], [72]. With a reference temperature of 290 K, their corresponding noise powers are -68.41 dBm and -74.61 dBm. As a result, the highest and lowest noise powers at the LNA (before amplification) are -67.9 dBm and -73.49 dBm, respectively, where the upper bound corresponds to the case of NF = 10 dB and temperature of 56.7°C, and the lower bound comes from the NF of 5 dB and temperature of -89.2°C, the corresponding SNR per bit E_b/N_0 is limited to [7, 1.38] dB. If the noise of the down-mixer is ignored, the system part after LNA shares the same SNR. The impact of S-parameters is tested with these two configurations in the experiment. Other non-ideal parameters, like non-linearity and phase noise, are excluded during the test. The result is given in Sec. VI-A.

Remark 6: The noise power generated by the transmitter could be ignored since it becomes very low due to the high propagation attenuation. E.g., in this system, the noise power that comes from the PA with an NF of 10 dB is −68.41 dBm, it is attenuated to −153.73 dBm after propagation, which is much lower than the contribution of the other noise sources.

Remark 7: To ensure the system performance only depends on the varied parameter, other parameters must be idealized. The ideal parameters in this work mean they have no impact on system performance. The ideal S-parameters have only a non-zero value of s_{21}. The ideal non-linearity means the corresponding component always works in a linear case, i.e., P_{sat}, P1dB, and IP3 are infinite. The NFs are set to zero when they are idealized. As for PN, the ideality means the phase noise level at all the frequency offsets is set to a very low value (e.g., −300 dBc/Hz), and its influence on communication and radar functions is negligible.

B. PHASE NOISE

The phase noise of the up/down-mixers mainly comes from the non-ideal oscillators. Ideal oscillators generate a pure sine wave whose spectrum is a Dirac delta function. However, realistic oscillators also generate noise, which extends the spectrum to wider bands [73]. This noise is mainly phase noise, whereas amplitude noise is considered negligible. Hence, for a sinusoidal wave, the output of the oscillator can be described by

$$v_{\text{o}}(t) = A \cdot \cos(2\pi f_{\text{c}} t + \phi_{\text{n}}(t)), \tag{17}$$

where A denotes the signal amplitude and $\phi_{\text{n}}(t)$ represents the phase noise. The phase noise appears as a jitter in the time domain and results in a broader spectrum in the frequency domain. Its unit is usually dBc/Hz, which denotes the noise power relative to the signal power in a 1 Hz bandwidth at a certain frequency offset from the carrier frequency. Generally, the PN at higher-frequency offsets is lower than at low-frequency offsets. For the mixers or oscillators, there always exists a noise floor for the PN, where the PN is white at the frequency offsets higher than a threshold, which is generally not higher than 10 MHz [74], [75], [76].

Not only the noise level but also the frequency offset of the PN plays an important role in the system degradation, i.e., the phase noise at different frequency offsets has different impacts on the system operation.

In the state-of-the-art literature [75], [76], different kinds of mixers with different PN values are proposed. All the mixers evaluated in this work are summarized in Tab. 4. In the following, the mixers 'mixer 1', 'mixer 2', and 'mixer 3' are denoted by 'this system', according to [76] and [75], respectively. The PN levels are specified for [10 kHz, 10 MHz], whereas the PN level at higher frequency offsets exhibits a noise floor, see Fig. 5. In the experiment, the impact of the PN on BER and MAEs is evaluated by varying the PN over different frequency offsets, while their phase noise level at 1 MHz and 10 MHz is recorded, since most state-of-the-art literature [67], [74], [75], [76] contribute on the phase noise

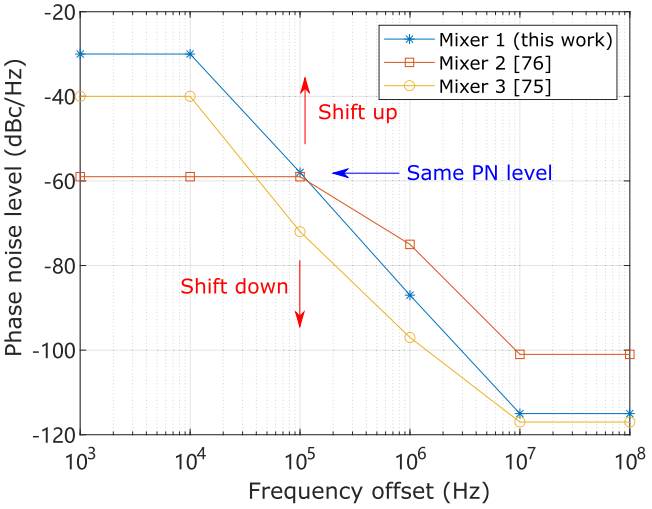

FIGURE 5. Phase noise of the three evaluated mixers at $f_{\text{c}} = 77$ GHz.

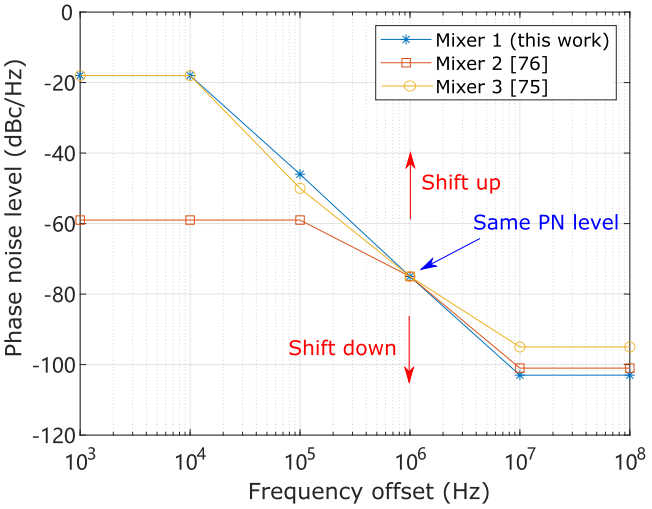

FIGURE 6. Exemplary evaluated phase noise curve for the three considered mixers, which were adapted to have the same noise level at 1 MHz (here: PN@1 MHz = −75 dBc/Hz at 77 GHz).

at these two frequencies. In the first step, the relationship between the system performance and the PN at 1 MHz is recorded: the mixers are adapted to have the same phase noise level at 1 MHz by vertical shifting, e.g., in Fig. 6, where their PN at 1 MHz is −75 dBc/Hz. During the tests, the PN lines are panned upwards and downwards. Consequently, the PN levels at different frequency offsets are changed in the same manner. The MAEs and BER versus PN at 1 MHz curves are analyzed. Other parameters (S-parameters, noise figure and non-linearities) are idealized during the tests, in order to reduce/eliminate their influence. Afterward, the same procedure is performed, but now for a PN held the same at 10 MHz (e.g., Fig. 7), corresponding to a change in the noise floor. The result is described in Sec. VI-B.

C. NON-LINEARITY OF THE AMPLIFIERS

The non-linear property of the amplifiers causes distortion since the components lose their linear behavior when the

TABLE 4. Phase noise of the three mixers at [0.01, 0.1, 1, 10] MHz.

Source	Mixer 1 (this system)	Mixer 2 [76]	Mixer 3 [75]
PN at [0.01,0.1,1,10] MHz in dBc/Hz	[-30,-58,-87,-115]	[-59,-59,-75,-101]	[-40,-72,-97,-117]

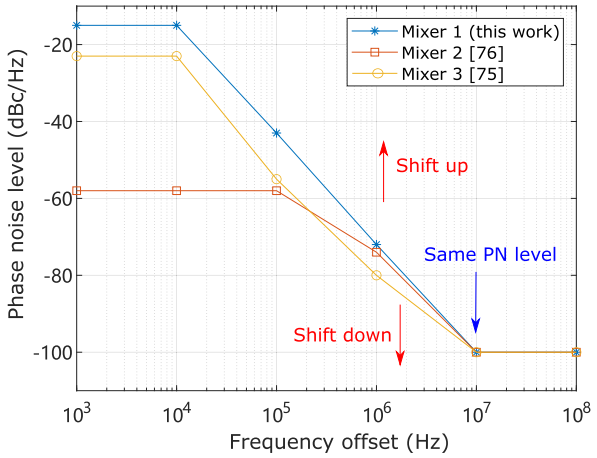

FIGURE 7. Exemplary evaluated phase noise curve for the three considered mixers, which were adapted to have the same noise level at 10 MHz, the equivalent of an identical noise floor (here: PN@10 MHz = −100 dBc/Hz at 77 GHz).

input signal approaches a certain threshold. The non-linearity parameters of the RF hardware mainly include the IP3, the P1dB and the output saturation power P_{sat}.

- IP3: the intercept point of the output power of the third-order non-linear and the fundamental linear terms. Generally, the IP3 is 10 dB higher than the P1dB [77]. However, the IP3 is a theoretical value since the output is saturated before approaching this point. Nevertheless, the IP3 is an important index as it indicates the linearity of the devices.
- P1dB: the output power level at which it is 1 dB less than the ideal linear output power. It is specified to prevent the device from running into compression and creating distortion due to the non-linearity properties.
- P_{sat}: the output saturation power, which corresponds to the maximum output power of the device.

As observed in [17], the non-linearity of PA has a significant impact on the JCRS system performance, since it directly affects the maximum transmission power. When the output signal power reaches the OP1dB, it starts to be suppressed, and as a result, distortions appear. However, for a PMCW system, since the data signal is phase shift keying (PSK)-modulated, the non-linear compression has no impact on its waveform. In this case, the non-linearity influences the system performance only by limiting the transmission power.

At the receiver side, if the received signal power is below the noise floor, the data transmission and radar sensing usually fail. Because there exist noise sources like LNA at the receiver side, it is necessary to guarantee a relatively high signal power level at the receiver side. This requires either reducing the path loss or increasing the transmission power. As the transmission power is mainly influenced by the configuration of PA, PA's P_{sat} is chosen to analyze the influence of the non-linear parameters on system performance. Other parameters, like OP1dB and IIP3, modify the signal waveform also by compressing its power and are not investigated in this work.

In the experiment, the following three cases are evaluated: ideal RF components, meaning that the other hardware parameters except for P_{sat} are idealized; sub-ideal components, in which only the non-ideal P_{sat} and noise source at the receiver (thermal noise, LNA NF) are included; and the non-ideal case, where all of the non-ideal parameters are integrated (channel noise and interference are still excluded). The BER and MAEs are compared for the above-mentioned three conditions. The impact of the non-linearity of PA is described in Sec. VI-C.

Remark 8: As described in Sec. III-B, the channel attenuation is 96.31 dB for the communications part and 118.44 dB for the sensing part. Apparently, there exists a significant difference between the communications and radar channels. Thus, when the radar estimation becomes invalid due to too-high attenuation, the BER is not necessarily influenced. In order to observe the influence of P_{sat} on both communications and radar sensing in the same interval, the communication range is tripled (to 60.84 m) in this work, meaning the communication signal is more attenuated (105.86 dB channel attenuation). With this configuration, both the communication and radar functions experience a transition from unreliable to reliable in the same interval (here: $P_{\text{sat}} \in [-8, 4]$ dBm, observed in the experiment). The same channel configuration is also utilized in the experiment of noise in the following sections.

D. NOISE

Since the RF components generate additional noise, their effect on the system performance has to be taken into account. The noise sources mainly include thermal noise, diffusion noise, shot noise, $1/f$ noise and quantum noise. Thermal noise is the most common one, its power is given by

$$P_{\text{n}} = kT\Delta f, \tag{18}$$

where $k \approx 1.38 \times 10^{-23}$ J/K is called the Boltzmann constant. The temperature of the resistor is denoted by T. $\Delta f = 4$ GHz corresponds to the signal bandwidth.

For an active RF device, like mixers or amplifiers, its output noise power is usually expressed by

$$P_{\text{n,out}} = Gk\Delta f(T_{\text{in}} + T_{\text{eff}}), \tag{19}$$

where G represents its power gain, $kT_{\text{in}}\Delta f$ is the input noise power, and $GkT_{\text{eff}}\Delta f$ denotes the noise power generated by the component. It is worth mentioning, that the effective noise temperature T_{eff} does not necessarily correspond to the actual

temperature of the hardware components, instead, it depends on the noise figure.

Generally, the noise figure is used to express the intrinsic noise level of the devices and is defined as the ratio of the SNR at the input and output port:

$$F = \frac{\mathrm{SNR_{in}}}{\mathrm{SNR_{out}}}. \tag{20}$$

In consequence, it can be expressed by the effective noise temperature

$$F = \frac{P_\mathrm{s}/P_\mathrm{n,in}}{G \cdot P_\mathrm{s}/P_\mathrm{n,out}} = \frac{G \cdot P_\mathrm{n,in} + P_\mathrm{n,g}}{G \cdot P_\mathrm{n,in}} = 1 + \frac{T_\mathrm{eff}}{T_0}, \tag{21}$$

where P_s is the input signal power, $P_\mathrm{n,in}$ and $P_\mathrm{n,out}$ denote the noise power at the input and output ports, respectively. $P_\mathrm{n,g}$ represents the noise generated by the component, whereas T_0 is defined as the effective input noise temperature or reference temperature. It is common to calculate the NF regarding a reference temperature of $T_0 = 290\,\mathrm{K}$.

Generally, the noise figure is used to express the ability of RF components to generate noise and thus, it is chosen as variable in the noise tests, recording the BER and MAEs versus NF curves. Since both transmitter and receiver include noise sources, it is worthwhile to investigate and compare their respective effects. To this end, the experiment on their NFs is implemented separately: When the NF of the transmitter is being tested, the NF of the receiver is set to zero and vice versa. For simplification, the NF of PA and LNA is used to represent the NF of the RF transmitter and receiver, respectively. Considering the effect of PA non-linearity on SNR [17], both NFs are evaluated with a relatively high (15.82 dBm) and a low (−4 dBm, assumed) PA saturation power.

Similar to the configuration for the non-linearity test, the distance for the communication is tripled, and other parameters except the NF and the PA P_sat are idealized. Additionally, the channel noise is excluded. Therefore, the system performance is only affected by the NF of the PA or the LNA and $P_\mathrm{sat,\,PA}$. In Sec. VI-D, the influence of noise figure is discussed in detail.

VI. RESULTS

In the following, the results of the above-mentioned evaluations of the hardware impairments and their impact on the communications and radar sensing performance are introduced. This includes the investigations of the impact of S-parameters, the non-linearity of the PA, the noise figure at the transmitter and receiver, and the noise in general.

A. INFLUENCE OF THE S-PARAMETERS

As explained in section V-A, the experiment for S-parameters is implemented in the case of $E_\mathrm{b}/N_0 = 1.38\,\mathrm{dB}$ and $E_\mathrm{b}/N_0 = 7\,\mathrm{dB}$, where the noise comes from thermal noise and LNA. The S-parameters of the up-mixer, PA, LNA and down-mixer are varied in the test. The impact of the RF components for all-non-ideal S-parameters and all-ideal S-parameters is compared. Moreover, the effect of the non-ideal S-parameters of the individual devices is investigated and compared with each other.

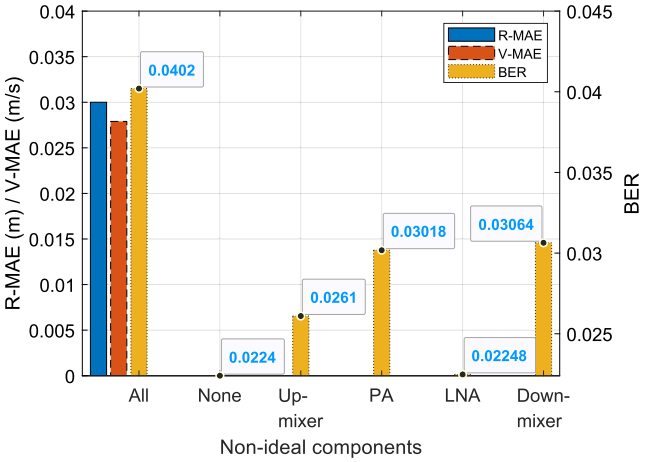

FIGURE 8. Impact of S-parameters on the sensing and communications performance in case of $E_\mathrm{b}/N_0 = 1.38\,\mathrm{dB}$.

Fig. 8 and Fig. 9 show the BER and the MAEs for both E_b/N_0 of 1.38 dB and 7 dB, respectively. The blue solid, red dashed and orange dotted bars represent the R-MAE, the velocity V-MAE and the BER, respectively. The R-MAE and V-MAE for different configurations are constant. Thus, they are only once expressed for the case 'all-non-ideal'.

The BER with all-ideal S-parameters is chosen as a fundamental line, and the impact of the devices is measured by the difference to this fundamental value, e.g., $\Delta\mathrm{BER_{PA}} = \mathrm{BER_{PA}} - \mathrm{BER_{none}}$ is used to measure the impact of PA. In Fig. 8, the ΔBER of all-non-ideal S-parameters and individual components are 0.0178, 0.0037, 0.0078, 0.0001 and 0.0082, respectively, where the sum of the ΔBER of the individual components is 0.0198, which is 0.002 higher than $\Delta\mathrm{BER_{all}}$ of 0.0178. The same phenomenon also exists in Fig. 9, where the sum ΔBER of the individual components is 0.0003, 0.00008 higher than the $\Delta\mathrm{BER_{all}}$ of 0.00022. In conclusion, the sum of the impacts of the individual S-parameters cannot be used to approach their co-influence.

The BER with all-non-ideal S-parameters is obviously higher than that with all-ideal S-parameters, meaning the non-ideal S-parameters have an impact on communications performance. However, the effect is very limited, since its impact on BER is negligible and cannot influence the sensing result. Additionally, different devices have different effects on communications reliability: in this system, the impacts, in descending order, are from down-mixer, PA, up-mixer, and LNA.

The S-parameters have no impact on the radar performance, since the MAEs with different configurations remain unchanged. Besides, the radar MAEs with the two SNRs are still the same, where the error is still within the radar resolution. The result indicates that the radar performance is more static to non-ideal S-parameters and noise than the communications performance. When facing non-ideal parameters and

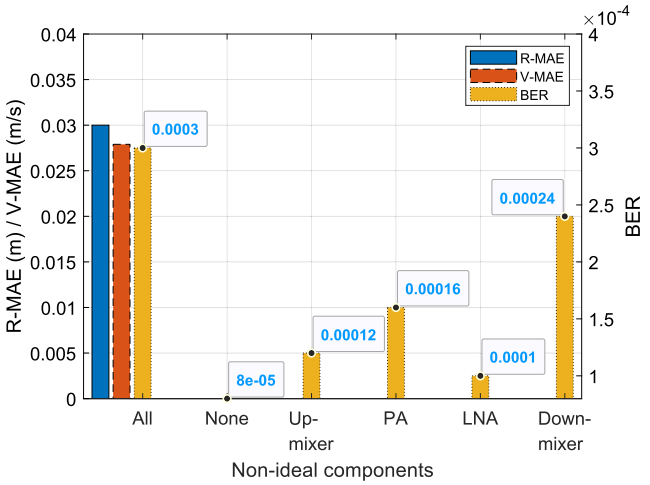

FIGURE 9. Impact of S-parameters on the sensing and communications performance in case of $E_b/N_0 = 7$ dB.

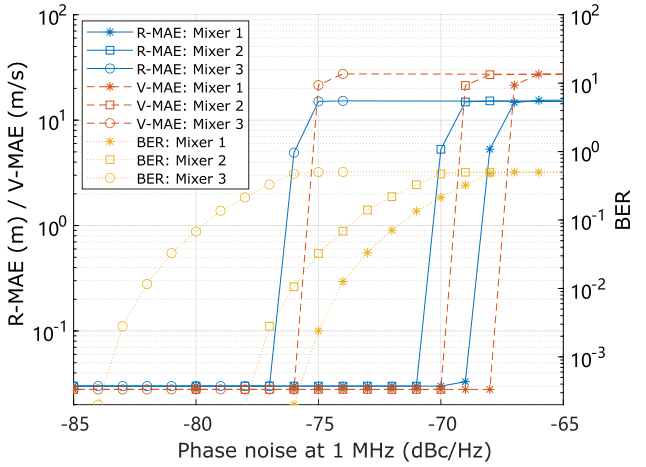

FIGURE 10. BER and MAEs with same PN levels at 1 MHz for $f_c = 77$ GHz.

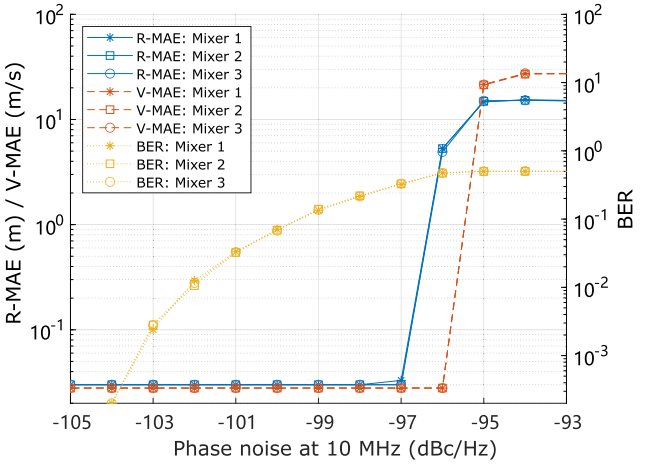

FIGURE 11. BER and MAEs with same PN levels at 10 MHz for $f_c = 77$ GHz.

noise, radar sensing is more reliable than communications. In conclusion, the impact of non-ideal S-parameters is negligible. It does not lead to significant performance degradation.

B. PHASE NOISE

The phase noise of the three mixers is varied in the experiment, while their values at 1 MHz and 10 MHz are recorded as $x-$values, and their impacts on BER and MAEs are compared. Fig. 10 and Fig. 11 show the results for the three mixers regarding the phase noise levels at 1 MHz and 10 MHz, respectively, where the corresponding intervals are $[-85, -65]$ dBc/Hz and $[-105, -93]$ dBc/Hz, respectively, since the transition of system performance from reliable to unreliable locates in this interval, observed in the experiment. The R-MAE, V-MAE and BER are denoted by the blue solid, red dashed and orange dotted lines, respectively. The asterisk, rectangular and circular markers denote the result for mixer 1, mixer 2 and mixer 3 (introduced in Tab. 4), respectively. It is obvious that the error increases with a higher PN level. With the increase of the phase noise level, the BER increases first, while the radar function is impacted only for higher phase noise levels. The upper bound of the BER and the MAEs arise from the binary random distribution of the data symbols: when the noise level is much higher than the signal, the results of the data detection and radar sensing become random variables. In consequence, the result of the data detection is a random variable and has a probability of $\Pr(X = 0) = \Pr(X = 1) = 0.5$ with a corresponding BER of 0.5. Besides, the values of the sensing MAEs are uniformly distributed in $[0, r_u]$ (the range/delay cannot be negative) and $[-v_u, v_u]$, respectively.

However, when the mixers are forced to have the same PN level at 1 MHz, they still exhibit different BERs and MAEs curves: mixer 1 has the most reliable performance against the phase noise, since its corresponding error increases with higher noise level than the other two mixers. Mixer 2 has the second-best performance and performs nearly the same as mixer 1 with a difference of 2 dBc/Hz. The third mixer is most sensitive to the phase noise and significantly differs from the other two mixers. The difference between the BER or MAEs of mixer 2 and mixer 3 is around 6 dBc/Hz.

The result indicates that the PN at 1 MHz is not dominant for the system performance degradation. Note that in Fig. 6, when the mixers are forced to have the same PN level at 1 MHz, mixer 1 has the lowest noise floor, mixer 2 has a noise floor comparable to that of mixer 1 with a difference of only 2 dBc/Hz, whereas mixer 3 has the highest noise floor, whose value is 6 dBc/Hz higher than mixer 2. This corresponds to their differences in Fig. 10. That is why it is necessary to investigate the phase noise at 10 MHz/ the impact of the noise floor in more detail.

Fig. 11 gives the result for the same PN level at 10 MHz, respectively the noise floor. Obviously, the three mixers have the same performance regardless of the difference in the PN at lower frequency offsets. This result indicates that the system performance is only influenced by the phase noise level at 10 MHz/the noise floor. For the designs of future JCRS systems, it is essential to choose mixers or oscillators with low phase noise levels at high-frequency bands.

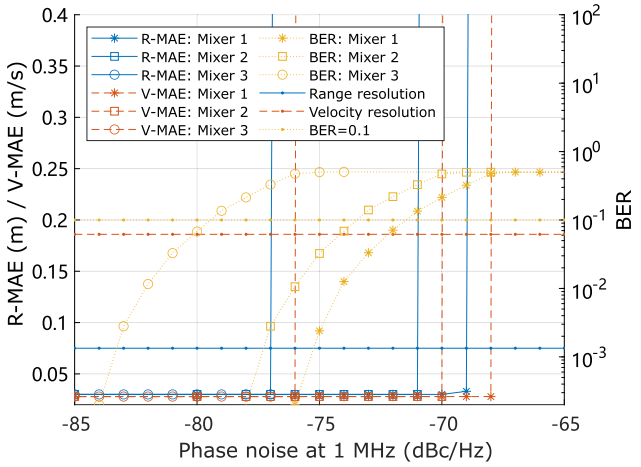

FIGURE 12. Reliable area of BER and MAEs with same PN levels at 1 MHz for $f_c = 77$ GHz.

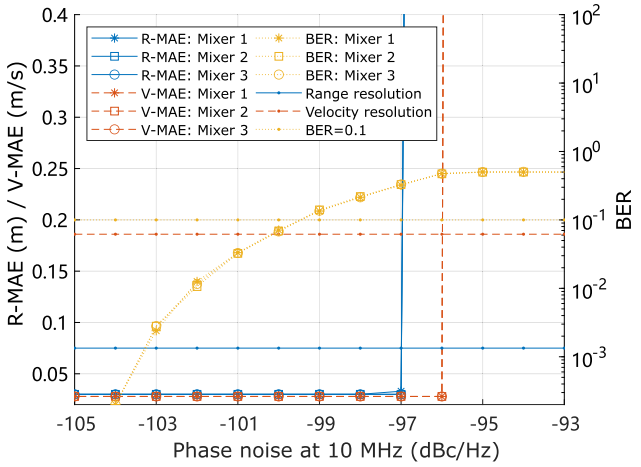

FIGURE 13. Reliable area of BER and MAEs with same PN levels at 10 MHz for $f_c = 77$ GHz.

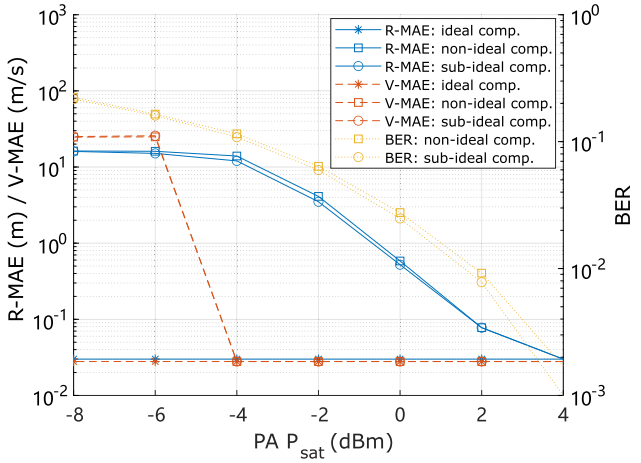

FIGURE 14. Impact of the PA's saturation power on the communications and sensing performance.

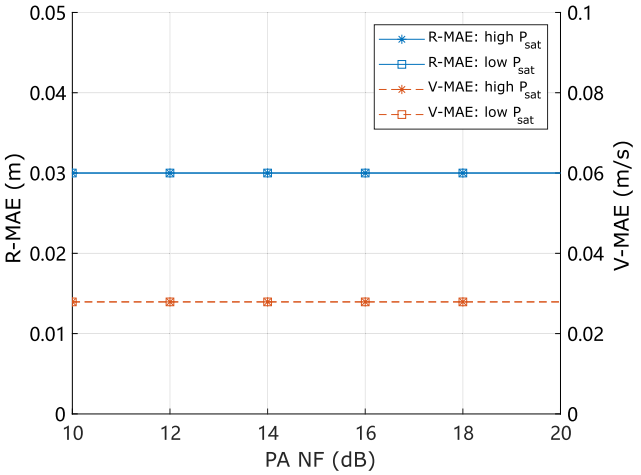

FIGURE 15. Impact of the PA's NF on the radar sensing performance. The BER is always 0 and thus, it is not included in this figure.

Additionally, the system behavior in the reliable operation area is zoomed in, since the users pay more attention to the real operation performance, as given in Fig. 12 and Fig. 13, where the newly added blue solid, red dashed and orange dotted horizontal lines without markers correspond to the range resolution, velocity resolution and the BER of 0.1. Obviously, when the PN level is low, the radar sensing error behaves as a constant and is limited in resolution, meaning the radar function in this interval is stable and reliable. However, the transition from a reliable operation to an unreliable one is extremely sharp, almost vertical to the $x-$axis. In this interval, even a change of 1 dBc/Hz leads to an invalid radar function. For the PMCW system, it would be better to guarantee that the phase noise floor is below -97 dBc/Hz. Actually, most state-of-the-art mixers, like those listed in Tab. 4, can satisfy this requirement.

C. NON-LINEARITY

Generally, the PA output saturation power and OP1dB are higher than 10 dBm, like the PA components proposed in [68], [78], [79], [80], and [81]. However, the high saturation power has no impact on the performance of this system, since the corresponding SNR at the receiver is too high. To observe an obvious impact, the saturation power is varied in the interval of $[-8, 4]$ dBm. The result is given in Fig. 14, where the R-MAE, the V-MAE and the BER are denoted by the blue solid, red dashed and orange dotted lines, respectively. The asterisk, rectangular and circular markers represent the result for ideal components, non-ideal components and sub-ideal components. Since there is no noise source, the SNR at the receiver for ideal components is always infinitive, the resulting BER is constant zero. It is not included in Fig. 14, as the BER is expressed in a log scale. Besides, the R-MAE and V-MAE for ideal components are also not affected by P_{sat} and are fixed at 0.03 m and 0.0279 m/s, within the radar resolution.

The result with non-ideal and sub-ideal components is influenced by PA's P_{sat}: The MAEs and the BER decrease with the increase of PA P_{sat}, meaning the higher PA saturation power leads to better system performance since the

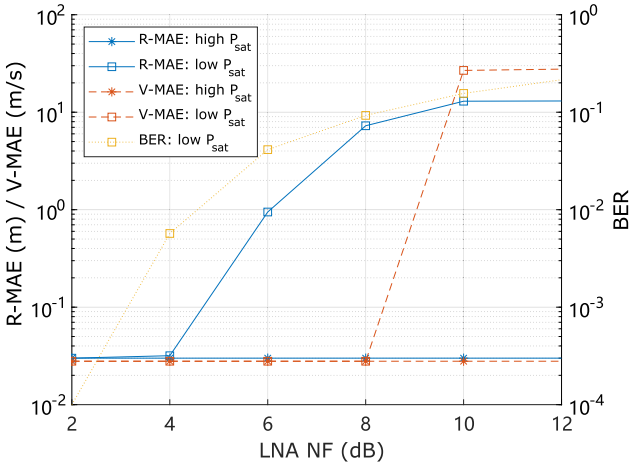

FIGURE 16. Impact of the LNA's NF on the communications and radar sensing performance.

non-linearity of PA directly determines the maximum transmission power. Besides, the result for non-ideal and sub-ideal components are almost the same. Considering the non-ideal components include all non-ideal parameters, where the latter only includes noise sources at the RF receiver, the result indicates that the noise generated at the receiver side is dominant in the system performance degradation when the transmission power is low. Moreover, the velocity estimation is the most robust against the variation of P_{sat}, i.e., SNR at the receiver side.

When the non-linearity parameters of the PA are too low, the noise at the receiver becomes the main factor that jeopardizes the system's performance. Thus, the high non-linearity parameters are desirable in PA and other hardware designs. Moreover, a highly linear transmitter can extend the available range for communications and sensing.

D. NOISE

As illustrated in Sec. VI-C, the noise generated at the receiver is one of the dominant factors in the system degradation, especially when the received signal power is low. In order to further confirm this conclusion, the influence of the noise generated at the transmitter and receiver sides is tested separately. The influence of the PA NF and the LNA NF are described in Fig. 15 and Fig. 16, respectively.

Since the noise figure of most state-of-the-art PAs is within [10, 20] dB [68], [78], [79], [80], and [81], in the experiment, the NF of the PA is varied in this interval, whereas the LNA NF is set to zero. In Fig. 15, the blue solid lines denote the R-MAEs, and the red dashed lines represent the V-MAEs. The lines with the asterisk and the rectangular markers show the result for $P_{\text{sat}} = 15.82$ dBm and -4 dBm, respectively. The number of error bits for all cases is still zero after 10^6 bits transmission, thus it is not indicated in this figure. Obviously, the R-MAE and V-MAE with different PAs P_{sat} are equal and remain constant as the PA's NF varies. The reason is that when the PA becomes the only noise source, the noise power at the PA output port is -31.6 dBm when NF equals 20 dB, which is much smaller than the PA's P_{sat}. After the channel propagation and attenuation, the SNR is still very high at the receiver. Therefore, the PA's NF has almost no effect on the system's performance. In conclusion, the noise generated at the transmitter side is not very essential to be considered.

Generally, the noise figure of LNAs is less than 10 dB [47], [69], [72]. In the test, the NF of the LNA is limited to [2, 12] dB. The MAEs and BER versus LNA NF curves are shown in Fig. 16. The blue solid, red dashed and orange dotted lines represent the R-MAE, the V-MAE and the BER, respectively. The lines with the asterisk and rectangular markers denote the result with high and low PA P_{sat}, respectively. Note that the BER for a high PA P_{sat} is always zero. Thus, it is not included in this graph.

Besides, the channel attenuation for the communications is 105.86 dB and 118.44 dB for the radar signal, while the antennas with a gain of 16.56 dBi are installed at both the Tx and Rx sides. The received signal powers at the communications and radar receiver are -56.92 dBm and -69.5 dBm for $P_{\text{sat}} = 15.82$ dBm, and -76.74 dBm and -89.32 dBm for $P_{\text{sat}} = -4$ dBm, respectively. According to Eq. 18 and Eq. 21, the noise power of the LNA with an NF varying in the range of [2, 12] dB is limited to $[-80.29, -66.24]$ dBm. The SNR at the receiver is relatively high in the case of the high PA saturation power. Thus in Fig. 16, the R-MAE and V-MAE keep constant and are limited in the radar resolution.

However, in the case of the low PA's P_{sat}, the useful signal power is not dominant at the receiver anymore. Consequently, the impact of LNA NF becomes significant, and the MAEs and the BER increase with an increasing noise figure. The velocity estimation has the best resistance to the noise since its error increases when the LNA's NF > 8 dB, while the range estimation becomes unreliable when the NF of the LNA is greater than 4 dB.

It follows that the noise source at the receiver has a much greater influence than that at the transmitter. When the received signal power is too low (due to low transmission power, high attenuation, etc.), the effect of the receiver noise becomes significant. According to the Friis formula for noise factors, the NF of the LNA is dominant at the receiver. Thus, reducing the LNA's NF and increasing the PA's non-linearity parameters would be good measures to extend the reliable communications and sensing range.

VII. DISCUSSION

This work focuses on the impact of the RF components on the JCRS system with the waveform of PMCW at 77 GHz. The impacts of the S-parameters, phase noise, non-linearity and noise figure are summarized:

- S-parameters: very inconspicuous influence on the system, cannot be a dominant factor in performance degradation.
- Phase noise: the phase noise of the mixers at 10 MHz and higher frequency offsets significantly impact system

reliability. The phase noise floor should be limited to below −97 dBc/Hz.
- Non-linearity: the non-linearity (especially for the PA) directly influences the transmission power, thus, is an important factor for system performance and available distance.
- Noise figure: generally, the NF at the transmitter side has no influence since the SNR is high. The NF at the receiver side (especially for the LNA) is essential for the system. When the received signal power is low (due to e.g., low transmission power, long distance, etc.), the noise figure has a significant impact on system reliability.

Bozorgi et al. [25] investigated the RF hardware challenges on the JCRS system with the waveform of FMCW. In their research, they mainly focus on the phase noise of the mixers, the non-linearity of the PA and the noise generated by the LNA:

- Mixers: for an FMCW system, the phase noise influences the range estimation, while the impact on velocity error is negligible because the range and velocity errors are proportional to the cosine and sine values of the channel delay τ, which is a very small value. However, the phase noise has an influence on both range and velocity estimation in a PMCW system, as discussed in this work.
- PA: as discussed in [25], the higher PA OP1dB, the more linear the transmitter. Generally, the modulated signals have high PAPR, and the corresponding PAs are required to work mostly at 6 dB back-off from their OP1dB to avoid distortion. Moreover, the PA non-linearity also limits the maximum available transmission power and thus, the radar sensing range. For a PMCW system, since the signal is PSK-modulated, the PAPR is 1, thus the non-linearity cannot cause distortion. Therefore, the PA can always work at maximum power without concern with the non-linear compression, extending the maximum sensing range and reliability, which is an advantage of PMCW.
- LNA: since the LNA is usually the first analog front-end device at the receiver, it is the dominant factor that affects the noise figure or SNR. For both FMCW and PMCW systems, the LNA's NF directly limits the maximum radar detection range. Additionally, it also influences the BER of communications.

Moreover, Mao et al. [35] designed a JCRS system with the waveform in mmWave and low-THz bands, where the impact of I/Q imbalance and LO phase noise of the mixers are considered. From their point of view, the mixers not only generate phase noise but also introduce image components, which is called I/Q imbalance. However, the image component is usually much smaller than the useful signal and thus, it could be ignored. Additionally, the researchers consider that for a mono-static radar transceiver, the phase noise of the up-mixer and down-mixer could cancel each other out when the propagation delay is sufficiently short since the mixers use the same oscillator. This measurement could be adopted in future works.

Moreover, studies to expand the current model to a multi-user system are ongoing. In this context, precoder-coder design to maximize the signal interference noise ratio like Cui et al. [82], and power allocation like in [83] are also discussed. Besides, we extend the analysis of hardware impairments, the same as Adler et al. [49] proposed. This includes the evaluation of mutual coupling between antenna elements, the transmit-receive isolation in multi-antenna arrays next to I/Q-imbalances, the amplifier non-linearities, the A/D and D/A-converters impairments or the phase noise.

Furthermore, various JCRS waveforms are under consideration. In consequence, we are working on the extension of our PMCW-CDMA-based model to also provide other JCRS models based on additional waveforms. Examples of such JCRS systems can be found for OFDM in [84] and [85], linear frequency modulation in [86], and combined waveforms like flexible sensing implanted-OFDM or orthogonal time frequency space in [87] and [13], respectively. And they are extended by space-frequency modulated co-designs, as proposed by Wang et al. in [88]. Especially, OFDM-based systems represent particularly interesting options. In this context, it has to be mentioned that the unfavorable behavior of OFDM regarding the PAPR is currently discussed in the literature and algorithms and approaches to reduce it are currently discussed [34], [89]. Further research in this area will form the basis for future work. Summarized, we want to extend our PMCW-CDMA model and compare it with other waveforms to obtain conclusions on the optimal waveform for JCRS applications.

VIII. CONCLUSION

In this work, a short-range JCRS system with the waveform of PMCW at 77 GHz is proposed. The RF components are shortly introduced and the impact of their parameters, including S-parameters, phase noise, non-linearity and noise figures, on system performance is investigated. To the best of the authors' knowledge, no research has so comprehensively investigated the impact of RF parameters on the JCRS systems, especially for the PMCW-based systems. Compared to related works [25] and [35], this work focuses more on getting results from experiments instead of theoretical analysis. Moreover, in order to observe the impact of the individual parameters without influence from other parameters and RF devices, the parameters except those being tested are idealized in the test. This setting guarantees that the observed BER and MAEs are only influenced by the corresponding parameter.

The results show that the S-parameters have a very limited impact on the system. In contrast, the phase noise at 10 MHz and higher frequency offsets can affect both the communications and radar functions in a PMCW system. The PA's

non-linearity and the LNA's noise figure play an essential role in changing the SNR at the receiver. Improving these two characteristics can help to extend the maximum sensing range of a JCRS system.

However, the I/Q imbalances are not considered in this work. With the I/Q imbalances, the mixers generate an image component, which is generally much smaller than the desired signal. In [35], the researchers consider that the image component has a negligible impact on the result. To verify this assumption could be a future research direction.

Besides, this work has no consideration of A/D and D/A converters. With the signal in mmWave, the high requirement on the sampling rate of A/D and D/A converters leads to high costs, especially for OFDM and PMCW. Compared to the former two waveforms, the FMCW only requires lower-rate converters, which is an advantage. To investigate the influence of A/D and D/A converters could be another future research direction.

Moreover, this work only focuses on the impact of the non-ideal parameters, while the measurement to mitigate their impacts and make the system more resilient against other challenges has yet to be proposed. In future research, system resilience and reliability should be taken into consideration.

ACKNOWLEDGMENT

(Maximilian Lübke and Yanpeng Su contributed equally to this work.)

REFERENCES

[1] Z. Xiao and Y. Zeng, "Waveform design and performance analysis for full-duplex integrated sensing and communication," *IEEE J. Sel. Areas Commun.*, vol. 40, no. 6, pp. 1823–1837, Jun. 2022.

[2] C. Waldschmidt, J. Hasch, and W. Menzel, "Automotive radar—From first efforts to future systems," *IEEE J. Microw.*, vol. 1, no. 1, pp. 135–148, Jan. 2021.

[3] L. G. de Oliveira, B. Nuss, M. B. Alabd, A. Diewald, M. Pauli, and T. Zwick, "Joint radar-communication systems: Modulation schemes and system design," *IEEE Trans. Microw. Theory Techn.*, vol. 70, no. 3, pp. 1521–1551, Mar. 2022.

[4] F. Liu, Y. Cui, C. Masouros, J. Xu, T. X. Han, Y. C. Eldar, and S. Buzzi, "Integrated sensing and communications: Toward dual-functional wireless networks for 6G and beyond," *IEEE J. Sel. Areas Commun.*, vol. 40, no. 6, pp. 1728–1767, Jun. 2022.

[5] T. Wild, V. Braun, and H. Viswanathan, "Joint design of communication and sensing for beyond 5G and 6G systems," *IEEE Access*, vol. 9, pp. 30845–30857, 2021.

[6] Y. Cui, F. Liu, X. Jing, and J. Mu, "Integrating sensing and communications for ubiquitous IoT: Applications, trends, and challenges," *IEEE Netw.*, vol. 35, no. 5, pp. 158–167, Sep. 2021.

[7] B. Paul, A. R. Chiriyath, and D. W. Bliss, "Survey of RF communications and sensing convergence research," *IEEE Access*, vol. 5, pp. 252–270, 2017.

[8] R. Thoma, T. Dallmann, S. Jovanoska, P. Knott, and A. Schmeink, "Joint communication and radar sensing: An overview," in *Proc. 15th Eur. Conf. Antennas Propag. (EuCAP)*, Mar. 2021, pp. 1–5.

[9] C. D. Ozkaptan, E. Ekici, and O. Altintas, "Adaptive waveform design for communication-enabled automotive radars," *IEEE Trans. Wireless Commun.*, vol. 21, no. 6, pp. 3965–3978, Jun. 2022.

[10] K. V. Mishra, M. R. B. Shankar, V. Koivunen, B. Ottersten, and S. A. Vorobyov, "Toward millimeter-wave joint radar communications: A signal processing perspective," *IEEE Signal Process. Mag.*, vol. 36, no. 5, pp. 100–114, Sep. 2019.

[11] C. Sturm, Y. L. Sit, G. Li, H. A. Vayghan, and U. Lubbert, "Automotive fast-chirp MIMO radar with simultaneous transmission in a Doppler-multiplex," in *Proc. 19th Int. Radar Symp. (IRS)*, Jun. 2018, pp. 1–6.

[12] F. Uysal, "Phase-coded FMCW automotive radar: System design and interference mitigation," *IEEE Trans. Veh. Technol.*, vol. 69, no. 1, pp. 270–281, Jan. 2020.

[13] M. F. Munir, A. Basit, W. Khan, A. Saleem, and A. Al-salehi, "A comprehensive study of past, present, and future of spectrum sharing and information embedding techniques in joint wireless communication and radar systems," *Wireless Commun. Mobile Comput.*, vol. 2022, pp. 1–25, Mar. 2022, doi: 10.1155/2022/9642849.

[14] T. S. Rappaport, Y. Xing, O. Kanhere, S. Ju, A. Madanayake, S. Mandal, A. Alkhateeb, and G. C. Trichopoulos, "Wireless communications and applications above 100 GHz: Opportunities and challenges for 6G and beyond," *IEEE Access*, vol. 7, pp. 78729–78757, 2019.

[15] T. Rappaport, R. Heath, R. Daniels, and J. Murdock, *Millimeter Wave Wireless Communications* (Communications Engineering and Emerging Technology Series from Ted Rappaport Series). Upper Saddle River, NJ, USA: Prentice-Hall, 2015.

[16] M. Lübke, J. Fuchs, V. Shatov, A. Dubey, R. Weigel, and F. Lurz, "Simulation environment of a communication system using CDMA at 77 GHz," in *Proc. Int. Wireless Commun. Mobile Comput. (IWCMC)*, Jun. 2020, pp. 1946–1951.

[17] M. Lübke, Y. Su, A. J. Cherian, J. Fuchs, A. Dubey, R. Weigel, and N. Franchi, "Full physical layer simulation tool to design future 77 GHz JCRS-applications," *IEEE Access*, vol. 10, pp. 47437–47460, 2022.

[18] M. Lübke, J. Fuchs, V. Shatov, A. Dubey, R. Weigel, and F. Lurz, "Combining radar and communication at 77 GHz using a CDMA technique," in *IEEE MTT-S Int. Microw. Symp. Dig.*, Nov. 2020, pp. 1–4.

[19] M. Lübke and Y. Su, "Full physical layer simulation tool in Simulink for modelling automotive JCRS PMCW-CDMA based systems," FAU Erlangen-Nürnberg, Erlangen, Germany, 4th Version, Tech. Rep., Mar. 2022, doi: 10.5281/ZENODO.7352183.

[20] X. Yang, M. Matthaiou, J. Yang, C.-K. Wen, F. Gao, and S. Jin, "Hardware-constrained millimeter-wave systems for 5G: Challenges, opportunities, and solutions," *IEEE Commun. Mag.*, vol. 57, no. 1, pp. 44–50, Jan. 2019.

[21] Q. Wu, J. Xu, Y. Zeng, D. W. K. Ng, N. Al-Dhahir, R. Schober, and A. L. Swindlehurst, "A comprehensive overview on 5G-and-beyond networks with UAVs: From communications to sensing and intelligence," *IEEE J. Sel. Areas Commun.*, vol. 39, no. 10, pp. 2912–2945, Oct. 2021.

[22] S. Bartoletti, H. Wymeersch, T. Mach, O. Brunnegard, D. Giustiniano, P. Hammarberg, M. F. Keskin, J. O. Lacruz, S. M. Razavi, J. Ronnblom, F. Tufvesson, J. Widmer, and N. B. Melazzi, "Positioning and sensing for vehicular safety applications in 5G and beyond," *IEEE Commun. Mag.*, vol. 59, no. 11, pp. 15–21, Nov. 2021.

[23] H. Wymeersch, D. Shrestha, C. M. de Lima, V. Yajnanarayana, B. Richerzhagen, M. F. Keskin, K. Schindhelm, A. Ramirez, A. Wolfgang, M. F. de Guzman, K. Haneda, T. Svensson, R. Baldemair, and S. Parkvall, "Integration of communication and sensing in 6G: A joint industrial and academic perspective," in *Proc. IEEE 32nd Annu. Int. Symp. Pers., Indoor Mobile Radio Commun. (PIMRC)*, Sep. 2021, pp. 1–7.

[24] M. A. Uusitalo, P. Rugeland, M. R. Boldi, E. C. Strinati, P. Demestichas, M. Ericson, G. P. Fettweis, M. C. Filippou, A. Gati, M.-H. Hamon, M. Hoffmann, M. Latva-Aho, A. Parssinen, B. Richerzhagen, H. Schotten, T. Svensson, G. Wikstrom, H. Wymeersch, V. Ziegler, and Y. Zou, "6G vision, value, use cases and technologies from European 6G flagship project Hexa-X," *IEEE Access*, vol. 9, pp. 160004–160020, 2021.

[25] F. Bozorgi, P. Sen, A. N. Barreto, and G. Fettweis, "RF front-end challenges for joint communication and radar sensing," in *Proc. 1st IEEE Int. Online Symp. Joint Commun. Sens.*, Feb. 2021, pp. 1–6.

[26] M. Goppelt, H.-L. Blocher, and W. Menzel, "Analytical investigation of mutual interference between automotive FMCW radar sensors," in *Proc. German Microw. Conf.*, 2011, pp. 1–4.

[27] F. Engels, P. Heidenreich, M. Wintermantel, L. Stacker, M. A. Kadi, and A. M. Zoubir, "Automotive radar signal processing: Research directions and practical challenges," *IEEE J. Sel. Topics Signal Process.*, vol. 15, no. 4, pp. 865–878, Jun. 2021.

[28] U. Chipengo, P. M. Krenz, and S. Carpenter, "From antenna design to high fidelity, full physics automotive radar sensor corner case simulation," *Modelling and Simulation in Engineering*, vol. 2018, pp. 1–19, Dec. 2018.

[29] P. Nallabolu and C. Li, "A frequency-domain spoofing attack on FMCW radars and its mitigation technique based on a hybrid-chirp waveform," *IEEE Trans. Microw. Theory Techn.*, vol. 69, no. 11, pp. 5086–5098, Nov. 2021.

[30] Z. Sun, S. Balakrishnan, L. Su, A. Bhuyan, P. Wang, and C. Qiao, "Who is in control? Practical physical layer attack and defense for mmWave-based sensing in autonomous vehicles," *IEEE Trans. Inf. Forensics Security*, vol. 16, pp. 3199–3214, 2021.

[31] S. H. Dokhanchi, B. S. Mysore, K. V. Mishra, and B. Ottersten, "A mmWave automotive joint radar-communications system," *IEEE Trans. Aerosp. Electron. Syst.*, vol. 55, no. 3, pp. 1241–1260, Jun. 2019.

[32] V. Giannini, D. Guermandi, Q. Shi, A. Medra, W. Van Thillo, A. Bourdoux, and P. Wambacq, "A 79 GHz phase-modulated 4 GHz-BW CW radar transmitter in 28 nm CMOS," *IEEE J. Solid-State Circuits*, vol. 49, no. 12, pp. 2925–2937, Dec. 2014.

[33] B.-J. Choi, E.-L. Kuan, and L. Hanzo, "Crest-factor study of MC-CDMA and OFDM," in *Proc. Gateway 21st Century Commun. Village, IEEE VTS 50th Veh. Technol. Conf.*, Sep. 1999, pp. 233–237.

[34] J. Rong, F. Liu, and Y. Miao, "Integrated radar and communications waveform design based on multi-symbol OFDM," *Remote Sens.*, vol. 14, no. 19, p. 4705, Sep. 2022. [Online]. Available: https://www.mdpi.com/2072-4292/14/19/4705

[35] T. Mao, J. Chen, Q. Wang, C. Han, Z. Wang, and G. K. Karagiannidis, "Waveform design for joint sensing and communications in millimeter-wave and low terahertz bands," *IEEE Trans. Commun.*, vol. 70, no. 10, pp. 7023–7039, Oct. 2022.

[36] S. Zhou, X. Liang, Y. Yu, and H. Liu, "Joint radar-communications co-use waveform design using optimized phase perturbation," *IEEE Trans. Aerosp. Electron. Syst.*, vol. 55, no. 3, pp. 1227–1240, Jun. 2019.

[37] B. M. Popovic, "Optimum sets of interference-free sequences with zero autocorrelation zones," *IEEE Trans. Inf. Theory*, vol. 64, no. 4, pp. 2876–2882, Dec. 2018.

[38] L. Reichardt, J. Maurer, T. Fügen, and T. Zwick, "Virtual drive: A complete V2X communication and radar system simulator for optimization of multiple antenna systems," *Proc. IEEE*, vol. 99, no. 7, pp. 1295–1310, Jul. 2011.

[39] N. Shirude, M. Gofane, and M. S. Panse, "Design and simulation of RADAR transmitter and receiver using direct sequence spread spectrum," *IOSR J. Electron. Commun. Eng.*, vol. 9, no. 3, pp. 56–65, 2014.

[40] L. Wang, R. Iida, and A. M. Wyglinski, "Vehicular network simulation environment via discrete event system modeling," *IEEE Access*, vol. 7, pp. 87246–87264, 2019.

[41] A. Dakic, M. Hofer, B. Rainer, S. Zelenbaba, L. Bernadó, and T. Zemen, "Real-time vehicular wireless system-level simulation," *IEEE Access*, vol. 9, pp. 23202–23217, 2021.

[42] S. Saponara and A. Gagliardi, "Modeling and analysis of 802.11 p physical layer for V2X connected transport systems considering harsh operating conditions and HW device performance," in *Proc. Int. Conf. Electr. Electron. Technol. Automot.*, Jul. 2018, pp. 1–6.

[43] X. A. F. Cabezas, M. C. P. Paredes, L. F. Urquiza-Aguiar, and D. J. Reinoso-Chisaguano, "PhySim-11 p: Simulation model for IEEE 802.11 p physical layer in MATLAB," *SoftwareX*, vol. 12, Jul. 2020, Art. no. 100580.

[44] A. Triwinarko, I. Dayoub, and S. Cherkaoui, "PHY layer enhancements for next generation V2X communication," *Veh. Commun.*, vol. 32, Dec. 2021, Art. no. 100385.

[45] J. A. Zhang, K. Wu, X. Huang, Y. J. Guo, D. Zhang, and R. W. Heath Jr., "Integration of radar sensing into communications with asynchronous transceivers," *IEEE Commun. Mag.*, vol. 60, no. 11, pp. 106–112, Nov. 2022.

[46] A. N. Barreto, T. M. Pham, S. George, P. Sen, and G. Fettweis, "Analysis of a chirp-based waveform for joint communications and radar sensing (JC&S) using non-linear components," in *Proc. 15th Eur. Conf. Antennas Propag. (EuCAP)*, Mar. 2021, pp. 1–5.

[47] M. Dudek, D. Kissinger, R. Weigel, and G. Fischer, "A millimeter-wave FMCW radar system simulator for automotive applications including nonlinear component models," in *Proc. 8th Eur. Radar Conf.*, 2011, pp. 89–92.

[48] H. Chen, S. R. Aghdam, M. F. Keskin, Y. Wu, S. Lindberg, A. Wolfgang, U. Gustavsson, T. Eriksson, and H. Wymeersch, "MCRB-based performance analysis of 6G localization under hardware impairments," in *Proc. IEEE Int. Conf. Commun. Workshops*, May 2022, pp. 115–120.

[49] J. Adler, T. Kronauer, and A. N. Barreto, "HermesPy: An open-source link-level evaluator for 6G," *IEEE Access*, vol. 10, pp. 120256–120273, 2022.

[50] C. Sommer, R. German, and F. Dressler, "Bidirectionally coupled network and road traffic simulation for improved IVC analysis," *IEEE Trans. Mobile Comput.*, vol. 10, no. 1, pp. 3–15, Jan. 2010.

[51] R. Riebl, H.-J. Gunther, C. Facchi, and L. Wolf, "Artery: Extending veins for VANET applications," in *Proc. Int. Conf. Models Technol. Intell. Transp. Syst.*, Jun. 2015, pp. 450–456.

[52] T. Zugno, M. Drago, M. Giordani, M. Polese, and M. Zorzi, "NR V2X communications at millimeter waves: An end-to-end performance evaluation," in *Proc. IEEE Global Commun. Conf.*, Dec. 2020, pp. 1–6.

[53] M. Drago, T. Zugno, M. Polese, M. Giordani, and M. Zorzi, "MilliCar: An ns-3 module for mmWave NR V2X networks," in *Proc. Workshop NS-3*, New York, NY, USA, Jun. 2020, pp. 9–16.

[54] C. R. Storck and F. Duarte-Figueiredo, "A 5G V2X ecosystem providing Internet of Vehicles," *Sensors*, vol. 19, no. 3, pp. 1–15, 2019. [Online]. Available: https://www.mdpi.com/1424-8220/19/3/550

[55] Z. Xinyu, "Analysis of M-sequence and gold-sequence in CDMA system," in *Proc. IEEE 3rd Int. Conf. Commun. Softw. Netw.*, May 2011, pp. 466–468.

[56] K. Singhal, "Walsh Codes, PN Sequences and their role in CDMA Technology," *Term Paper, EEL*, vol. 201, pp. 1–4, Jan. 2012.

[57] K.-U. Schmidt, "Sequences with small correlation," *Des., Codes Cryptogr.*, vol. 78, no. 1, pp. 237–267, 2016.

[58] D. Torrieri, *Principles of Spread-Spectrum Communication Systems*, vol. 1. Cham, Switzerland: Springer, 2005.

[59] M. Lübke, J. Fuchs, A. Dubey, H. Hamoud, F. Dressler, R. Weigel, and F. Lurz, "Validation and analysis of the propagation channel at 60 GHz for vehicular communication," in *Proc. IEEE 94th Veh. Technol. Conf.*, Sep. 2021, pp. 1–7.

[60] J. Hatch, A. Topak, R. Schnabel, T. Zwick, R. Weigel, and C. Waldschmidt, "Millimeter-wave technology for automotive radar sensors in the 77 GHz frequency band," *IEEE Trans. Microw. Theory Techn.*, vol. 60, no. 3, pp. 845–860, Mar. 2012.

[61] Z. Ni, J. A. Zhang, X. Huang, K. Yang, and F. Gao, "Parameter estimation and signal optimization for joint communication and radar sensing," in *Proc. IEEE Int. Conf. Commun. Workshops*, Jun. 2020, pp. 1–6.

[62] F. Liu, C. Masouros, A. P. Petropulu, H. Griffiths, and L. Hanzo, "Joint radar and communication design: Applications, state-of-the-art, and the road ahead," *IEEE Trans. Commun.*, vol. 68, no. 6, pp. 3834–3862, Jun. 2020.

[63] A. Bourdoux, U. Ahmad, D. Guermandi, S. Brebels, A. Dewilde, and W. Van Thillo, "PMCW waveform and MIMO technique for a 79 GHz CMOS automotive radar," in *Proc. IEEE Radar Conf. (RadarConf)*, May 2016, pp. 1–5.

[64] F. Roos, J. Bechter, C. Knill, B. Schweizer, and C. Waldschmidt, "Radar sensors for autonomous driving: Modulation schemes and interference mitigation," *IEEE Microw. Mag.*, vol. 20, no. 9, pp. 58–72, Sep. 2019.

[65] O. F. García, "Signal processing for mmWave mimo radar," M.S. thesis, Dept. Electron., Math. Natural Sci., Univ. Gävle, Gävle, Sweden, 2015.

[66] A. Behravan, R. Baldemair, S. Parkvall, E. Dahlman, V. Yajnanarayana, H. Bjorkegren, and D. Shrestha, "Introducing sensing into future wireless communication systems," in *Proc. 2nd IEEE Int. Symp. Joint Commun. Sens.*, Mar. 2022, pp. 1–5.

[67] Y. S. Lin, W. C. Wen, and C. C. Wang, "13.6 mW 79 GHz CMOS up-conversion mixer with 2.1 dB gain and 35.9 dB LO-RF isolation," *IEEE Microw. Wireless Compon. Lett.*, vol. 24, no. 2, pp. 126–128, Feb. 2014.

[68] L. Chen, L. Zhang, and Y. Wang, "A 26.4-dB gain 15.82-dBm 77-GHz CMOS power amplifier with 15.9% PAE using transformer-based quadrature coupler network," *IEEE Microw. Wireless Compon. Lett.*, vol. 30, no. 1, pp. 78–81, Jan. 2020.

[69] S. Li, T. Chi, D. Jung, T.-Y. Huang, M.-Y. Huang, and H. Wang, "An E-band high-linearity antenna-LNA front-end with 4.8 dB NF and 2.2 dBm IIP3 exploiting multi-feed on-antenna noise-canceling and Gm-boosting," in *IEEE Int. Solid-State Circuits Conf. (ISSCC) Dig. Tech. Papers*, Feb. 2020, pp. 1–3.

[70] J.-H. Lee, J. M. Lee, and K. C. Hwang, "Series feeding rectangular microstrip patch array antenna for 77 GHz automotive radar," in *Proc. Int. Symp. Antennas Propag. (ISAP)*, Oct. 2017, pp. 1–2.

[71] H. T. Friis, "Noise figures of radio receivers," *Proc. IRE*, vol. 32, no. 7, pp. 419–422, Jul. 1944.

[72] B. Wang, H. Gao, A. R. van Dommele, M. K. Matters-Kammerer, and P. G. M. Baltus, "60-GHz low-noise VGA and interpolation-based gain cell in a 40-nm CMOS technology," *IEEE Trans. Microw. Theory Techn.*, vol. 67, no. 2, pp. 518–532, Feb. 2019.
[73] D. Owen. (May 2004). *Good Practice Guide to Phase Noise Measurement*. Measurement Good Practice Guide. [Online]. Available: http://eprintspublications.npl.co.uk/3519/
[74] F. Starzer, C. Wagner, D. Lukashevich, H.-P. Forstner, L. Maurer, and A. Stelzer, "An area and phase noise improved 19-GHz down-converter VCO for 77-GHz automotive radar frontends in a SiGe bipolar production technology," in *Proc. IEEE Bipolar/BiCMOS Circuits Technol. Meeting*, Oct. 2008, pp. 113–116.
[75] F.-W. Kuo, Z. Zong, H.-N.-R. Chen, L.-C. Cho, C.-P. Jou, M. Chen, and R. B. Staszewski, "A 77/79-GHz frequency generator in 16-nm CMOS for FMCW radar applications based on a 26-GHz oscillator with co-generated third harmonic," in *Proc. IEEE 45th Eur. Solid State Circuits Conf. (ESSCIRC)*, Sep. 2019, pp. 53–56.
[76] S.-K. Kim, C. Cui, S. Nam, and B.-S. Kim, "A low-power 77 GHz transceiver for automotive radar system in 65 nm CMOS technology," in *Proc. Asia–Pacific Microw. Conf. Proc. (APMC)*, Nov. 2013, pp. 236–238.
[77] A. Doerry, "Component and circuit performance measurements for coherent radar—A systems perspective," Sandia, Albuquerque, NM, USA, Tech. Rep. SAND-2020-5228;686268, 2020.
[78] K.-L. Wu, K.-T. Lai, R. Hu, C. F. Jou, D.-C. Niu, and Y.-S. Shiao, "77–110 GHz 65-nm CMOS power amplifier design," *IEEE Trans. Terahertz Sci. Technol.*, vol. 4, no. 3, pp. 391–399, May 2014.
[79] G. Wu, Y. Zhang, L. He, D. Gao, Y. Liu, Y. Guo, and H. Gao, "A 77 GHz power amplifier design with in-phase power combing for 20 dBm psat in a 40-nm CMOS technology," in *Proc. IEEE Int. Symp. Circuits Syst. (ISCAS)*, May 2021, pp. 1–4.
[80] L. Wang, J. Borngraeber, W. Winkler, and C. Scheytt, "A 77-GHz MMIC power amplifier driver for automotive radar," in *Proc. IET Int. Conf. Radar Syst.*, 2007, pp. 1–2.
[81] V.-S. Trinh and J.-D. Park, "A 16.4-dBm 20.3% PAE 22-dB gain 77 GHz power amplifier in 65-nm CMOS technology," *IEEE Access*, vol. 9, pp. 159541–159548, 2021.
[82] Y. Cui, V. Koivunen, and X. Jing, "Precoder and decoder co-designs for radar and communication spectrum sharing," *Sensors*, vol. 22, no. 7, p. 2619, Mar. 2022. [Online]. Available: https://www.mdpi.com/1424-8220/22/7/2619
[83] Y. Liu, Z. Wei, C. Yan, Z. Feng, and G. L. Stuber, "Effective capacity based power allocation for the coexistence of an integrated radar and communication system and a commercial communication system," *IEEE Access*, vol. 8, pp. 58629–58644, 2020.
[84] T. Xu, F. Liu, C. Masouros, and I. Darwazeh, "An experimental proof of concept for integrated sensing and communications waveform design," *IEEE Open J. Commun. Soc.*, vol. 3, pp. 1643–1655, 2022.
[85] A. Ahmed, Y. D. Zhang, and A. Hassanien, "Joint radar-communications exploiting optimized OFDM waveforms," *Remote Sens.*, vol. 13, no. 21, p. 4376, Oct. 2021. [Online]. Available: https://www.mdpi.com/2072-4292/13/21/4376
[86] H. Ma, J. Wang, X. Sun, T. Hou, and W. Jin, "Joint radar-communication relying on NLFM-MSK design," *Wireless Commun. Mobile Comput.*, vol. 2022, pp. 1–26, Jan. 2022, doi: 10.1155/2022/4711132.
[87] Y. Mal, Z. Yuan, G. Yu, S. Xia, and L. Hu, "A spectrum efficient waveform integrating OFDM and FMCW for joint communications and sensing," in *Proc. IEEE Int. Conf. Commun. Workshops (ICC Workshops)*, May 2022, pp. 475–479.
[88] Z. Wang, G. Liao, and Z. Yang, "Space-frequency modulation radar-communication and mismatched filtering," *IEEE Access*, vol. 6, pp. 24837–24845, 2018.
[89] J. Rong, F. Liu, and Y. Miao, "High-efficiency optimization algorithm of PMEPR for OFDM integrated radar and communication waveform based on conjugate gradient," *Remote Sens.*, vol. 14, no. 7, p. 1715, Apr. 2022. [Online]. Available: https://www.mdpi.com/2072-4292/14/7/1715

MAXIMILIAN LÜBKE (Member, IEEE) received the B.Sc. degree in medical engineering and the M.Sc. degree in electrical engineering from Friedrich-Alexander-Universität Erlangen-Nürnberg (FAU), Erlangen, Germany, in 2017 and 2018, respectively. In 2019, he joined the Institute for Electronics Engineering, FAU, as a Research Assistant. In 2022, he switched to the Chair of Electrical Smart City Systems. His current research interests include joint radar and communication systems and circuit design with respect to automotive applications. He was a recipient of the Best Paper Award of the ACM International Conference on Nanoscale Computing and Communication, in 2019, and the EAI International Conference on Bio-Inspired Information and Communications Technologies, in 2020.

YANPENG SU (Member, IEEE) received the B.Sc. degree in electrical engineering and automation from the China University of Petroleum (East China) (UPC), Qingdao, China, in 2018, and the M.Sc. degree in electrical engineering from Friedrich-Alexander-Universität Erlangen-Nürnberg (FAU), Erlangen, Germany, in 2022. In 2022, he joined the Chair of Electrical Smart City Systems, FAU, as a Research Assistant. His research interests include joint radar and communication systems and resilient communications.

NORMAN FRANCHI (Member, IEEE) received the Dr.-Ing. (Ph.D.E.E.) and Dipl.-Ing. (M.S.E.E.) degrees in electrical, electronic, and communications engineering (EEI), in 2015 and 2007, respectively. He is a Full Professor (W3) with Friedrich-Alexander-Universität Erlangen-Nürnberg, Germany, where he heads the Chair of Electrical Smart City Systems. From 2007 to 2011, he was with the Automotive Research and Development Sector, as a System and Application Engineer of advanced networked control system design. From 2012 to 2015, he was a Research Associate with the Institute for Electronics Engineering, FAU, Germany, focused on software-defined radio-based V2X communications. From 2015 to 2021, he was with Gerhard Fettweis' Vodafone Chair, Dresden University of Technology (TU Dresden), where he was a Senior Research Group Leader of resilient mobile communications systems and 5G industrial campus networks. From 2019 to 2020, he was a Managing Director of the 5G Laboratory GmbH, Germany. In 2020, he founded the company Advancing Individual Networks (AIN) GmbH, Germany, a technology start-up for the design, optimization, and operation of IIoT networks. He is a member of the IEEE ISAC initiative, Open 6G Hub Germany, 5G Lab Germany, and 6G Platform Germany. Furthermore, he is an advisory board member of the Industrial Radio Laboratory Germany (IRLG) and the KI Park Deutschland. His research interests include 6G, joint communications and sensing, resilient and secure systems, IIoT, open RAN, V2X, and green ICT for smart cities.